Contents lists available at ScienceDirect

Ecological Indicators

Deciphering the potential of Ba/Ca, Mo/Ca and Li/Ca profiles in the bivalve shell *Pecten maximus* as proxies for the reconstruction of phytoplankton dynamics

Lukas Fröhlich [a],[*], Valentin Siebert [b], Qian Huang [a], Julien Thébault [b], Klaus Peter Jochum [c], Bernd R. Schöne [a]

[a] *Institute of Geosciences, University of Mainz, Johann-Joachim-Becher-Weg 21, 55128 Mainz, Germany*
[b] *Univ Brest, CNRS, IRD, Ifremer, LEMAR, F-29280 Plouzané, France*
[c] *Climate Geochemistry Department, Max Planck Institute for Chemistry, P.P. Box 3060, 55020 Mainz, Germany*

ARTICLE INFO

ABSTRACT

Shells of the fast-growing bivalve *Pecten maximus* serve as a geochemical archive for the reconstruction of past phytoplankton dynamics. Specifically, high-resolution, temporally accurately aligned molar barium-to-calcium (Ba/Ca_{shell}), molybdenum-to-calcium (Mo/Ca_{shell}) and lithium-to-calcium ratios (Li/Ca_{shell}) of the shell calcite revealed distinct peaks which are closely linked to phytoplankton dynamics. Yet, the development and applicability of these geochemical proxies is still at an early stage and needs further calibration. In this study, we examined the relationship between the timing and magnitude of Ba/Ca_{shell}, Mo/Ca_{shell} and Li/Ca_{shell} peaks of *P. maximus* and the occurrence of various phytoplankton species (diatoms and dinoflagellates) from a statistical perspective. Studied shell samples (three specimens per calendar year) as well as detailed phytoplankton observation data were derived from the well-studied costal ecosystem of the Bay of Brest (France) over three years (2011, 2012 and 2019). An algorithm-based pseudo-random sampling simulation technique was established that analyzed the complex phytoplankton datasets with respect to the profiles of Ba/Ca_{shell}, Mo/Ca_{shell} and Li/Ca_{shell} to identify potential patterns between phytoplankton and trace element time-series. The simulation results indicate that the timing and magnitude of Ba/Ca_{shell}, Mo/Ca_{shell} and Li/Ca_{shell} peaks agreed best with the occurrence of specific phytoplankton blooms that developed ca. one to two weeks earlier. The data suggest that the formation of transient Ba/Ca_{shell} peaks had a plurispecific origin, i.e., potentially linked to blooms of ingestible diatom, dinoflagellate and flagellate species enriched in Ba that occurred 8 to 12 days earlier. Observed peaks in Mo/Ca_{shell} profiles demonstrably followed the timing and intensity of blooms of the dominant dinoflagellate genus *Gymnodinium* spp. after a short time lag of around 8 days, potentially linked to an enhanced enzyme activity of nitrate reductase that requires the presence of Mo in the dinoflagellate cells. In addition, Mo/Ca_{shell} peaks agreed with periods of diatom aggregate formation which were hypothesized to induce the formation of Mo/Ca_{shell} peaks in scallop shells. Li/Ca_{shell} profiles revealed similar patterns as large blooms of the diatom *Chaetoceros* spp. as well as to neurotoxin producing diatoms of the genus *Pseudo-nitzschia* when considering a short time lag of 8 to 12 days. These findings highlight the great potential of using Ba/Ca_{shell}, Mo/Ca_{shell} and Li/Ca_{shell} chronologies in *P. maximus* shells as proxies of past phytoplankton dynamics.

1. Introduction

Marine phytoplankton form the foundation of marine food webs and contribute considerably to global photosynthetic CO_2 fixation and oxygen production (e.g., Iglesias-Rodriguez et al., 2008; Shuter, 1979; Sigman and Boyle, 2000; Westberry et al., 2008). Despite accounting for<1 % of the total photosynthetic biomass, marine phytoplankton contribute to nearly half of the global net primary production (Field et al., 1998). Coastal habitats are among the most precious ecosystems (Barbier et al., 2011) that provide food for millions of people. However, these systems are increasingly threatened by climate change (e.g., ocean warming and acidification; Wiltshire and Manly, 2004; Winder and

Sommer, 2012) and other anthropogenic influences (e.g., over-exploitation, increased nutrient inputs from artificial fertilizers and pollutants; Beman et al., 2005; Del Amo et al., 1997; Nixon, 1995; Smith, 2003), leading to changes in phytoplankton community structures and dynamics (Hare et al., 2007; Marinov et al., 2010) as well as a loss in biodiversity (Cardinale et al., 2006; Worm et al., 2006). One consequence is the shift from a diatom-dominated ecosystem to one dominated by non-siliceous phytoplankton groups such as dinoflagellates (Cloern, 2001; Radach et al., 1990; Ragueneau et al., 1994), which can have negative impacts on fisheries and food webs due to toxic algal blooms. Accounting for these changes in phytoplankton dynamics over time is essential for the reliable modeling of potential future trends of marine ecosystems.

Detailed and long-term records of phytoplankton dynamics are sparse and limited to a few localities (e.g., Chauvaud et al., 2000; Richardson and Heilmann, 1995; Warner and Hays, 1994). Remotely sensed observations (e.g., Gordon et al., 1980; Hovis et al., 1980) provide a large spatial coverage but cannot be used to assess phytoplankton community structures on a higher taxonomic level (e.g., species) and are only available since a few decades. Traditional microscopic in-situ analyses as well as high-performance liquid chromatography of biochemical markers (e.g., carotenoid pigments) allow to evaluate phytoplankton community compositions on a fine temporal scale (e.g., Lionard et al., 2008; Wang et al., 2021; Wright et al., 2010), but are less useful to reconstruct past phytoplankton dynamics. A variety of tools are used to assess pre–industrial primary production, e.g., the biogeochemical analysis of marine sediments including barite precipitation rates, aluminum-to-titanium and barium-to-titanium ratios (e.g., Bishop, 1988; Dehairs et al., 1980; Dymond et al., 1997). However, these data only provide a limited temporal resolution that is insufficient to identify short-term phytoplankton events (days to weeks). Mollusk shells potentially provide a more suitable archive for this purpose as they record prevailing environmental conditions in the form of geochemical properties over seasons, years, decades or even centuries. These geochemical data can be temporally constrained by growth pattern analysis (Hallmann et al., 2008; Richardson et al., 1980; Schöne, 2008). To reconstruct phytoplankton dynamics, several studies used shells of the short-lived (up to ca. 12 years) bivalve, *Pecten maximus* (e. g., Barats et al., 2010; Chauvaud et al., 2011; Gillikin et al., 2008; Tabouret et al., 2012; Thébault et al., 2022). Especially during their second year of life (after the first winter growth cessation), these bivalves form distinct daily increments allowing to retrieve highly-resolved time-series (e.g., Chauvaud et al., 2005) that provide an ideal temporal resolution for assessing short-term phytoplankton events. Transient peaks in trace element profiles of barium (Ba), molybdenum (Mo) and lithium (Li) occurring synchronously among contemporaneous *P. maximus* shells were proposed to originate from food sources (e.g., Barats et al., 2010, 2009; Gillikin et al., 2008; Thébault et al., 2009; Thébault and Chauvaud, 2013). The formation of molar barium-to-calcium (Ba/Ca$_{shell}$) peaks are induced by the ingestion of Ba-rich diatom frustules rather than by an increase in the dissolved Ba concentration of the ambient water (Barats et al., 2009; Gillikin et al., 2008, 2006) or by enhanced riverine inputs (Thébault et al., 2009). While Ba/Ca$_{shell}$ profiles do not correlate strongly with bulk phytoplankton variations, Ba/Ca$_{shell}$ peaks correspond to the timing of blooms of individual phytoplankton species when applying a short time lag of several days (Fröhlich et al., 2022). Given the large inter-taxa variability in phytoplankton cell-associated Ba (Fisher et al., 1991; Martin and Knauer, 1973; Roth and Riley, 1971), it is hypothesized that various taxa contribute differently to the measured Ba/Ca$_{shell}$ peaks (Fröhlich et al., 2022; Thébault et al., 2009). Yet, further studies are needed to test this hypothesis. Similar to Ba enrichments in shells, molar molybdenum-to-calcium (Mo/Ca$_{shell}$) peaks are considered to have a dietary origin (Tabouret et al., 2012). According to Thébault et al. (2022), the formation of Mo/Ca$_{shell}$ peaks in scallop shells could be induced by the ingestion of Mo-rich diatom aggregates forming during periods of

nutrient limitation. Molar lithium-to-calcium (Li/Ca$_{shell}$) peaks have been associated with blooms of diatoms that adsorb dissolved Li from the water column onto their frustules and as such transport large quantities of Li to the site of calcification when digested by the bivalves (Thébault et al., 2022; Thébault and Chauvaud, 2013). Thus, peaks of Ba/Ca$_{shell}$, Mo/Ca$_{shell}$ and Li/Ca$_{shell}$ in scallop shells were demonstrably linked to phytoplankton dynamics, but the mechanisms controlling the formation of trace element peaks are still poorly understood. To improve the applicability of Ba/Ca$_{shell}$, Mo/Ca$_{shell}$ and Li/Ca$_{shell}$ as reliable indicators for past phytoplankton dynamics using fossil or subfossil shells, it is necessary to further disentangle the relationship between phytoplankton on a species level and the formation of trace element peaks in *P. maximus* shells.

This study analyzed the direct relationship between three years of highly resolved Ba/Ca$_{shell}$, Mo/Ca$_{shell}$ and Li/Ca$_{shell}$ profiles and the contemporaneous phytoplankton dynamics in the Bay of Brest, France. Diatoms and dinoflagellate species were shown to be the dominant phytoplankton taxa in the studied coastal ecosystem and are the main food source for the studied bivalve. Therefore, the analyses conducted herein focused primarily on the dynamics of diatom and dinoflagellate species. The objective of this work was to examine whether the formation of transient trace element peaks could be related to the occurrence of short-term phytoplankton events and whether a monospecific or a plurispecific connection exists. To identify patterns within the largely unknown relationship between phytoplankton dynamics and trace element profiles in scallop shells, a pseudo–random sampling method was used that calculated millions of possible phytoplankton combinations at various hypothetical time lags. This computational approach allowed to evaluate a complex ecosystem and its potential responses in shell geochemistry from a statistical perspective and adds information required for the interpretation of Ba/Ca$_{shell}$, Mo/Ca$_{shell}$ and Li/Ca$_{shell}$ profiles as proxies for past phytoplankton dynamics. Deciphering this link will help to further improve the applicability of shells of *P. maximus* as powerful and highly resolved geochemical archives.

2. Material and methods

2.1. Sampling locality, shell collection and preparation

Nine living specimens of *P. maximus* were collected by SCUBA divers at Lanvéoc (48°17'N 4°30'W), Bay of Brest, Brittany, northwest France (Fig. 1). The bay (ca. 180 km^2), a semi-enclosed ecosystem, is characterized as a macrotidal regime and an average water depth of 8 m. The sampling locality, Lanvéoc, is situated in the southern area, close to the Aulne river (Fig. 1). Three scallop shells were collected on 30 August 2011, three on 23 October 2012 and three specimens on 15 November 2019 (Table 1) and stored at −20 °C. All shells experienced one winter growth cessation. In order to prepare the shells for elemental analyses, all specimens were gently cleaned with tap water using a plastic brush, and epibionts were removed after dissecting each specimen. In this study, sclerochronological analyses were performed on the surface of the left (flat) valves (Fig. 2) that were rinsed ultrasonically for 3 min with deionized water to remove sediment trapped between adjacent striae.

2.2. LA-ICP-MS analysis

In-situ chemical analyses were performed on the surface of the shell sections that were cut along the axis of maximum growth (Fig. 2) using a handheld drill equipped with a 150 μm-thin disk (disk with galvanically bonded diamonds; Komet – Dental Gebr. Brasseler GmbH & Co. KG; Art.–No.: 6911H.-104.220). After cutting, the shell slabs were immersed in acetic acid (10 vol%) for ca. 1 min and thoroughly rinsed using deionized water, to remove potential surface contamination. All shell samples were analyzed for their Ba (measured as ^{137}Ba), Mo (^{97}Mo) and Li (^{7}Li) content using a Laser Ablation – Inductively Coupled Plasma – Mass Spectrometer (LA-ICP-MS) system at the Max Planck Institute for
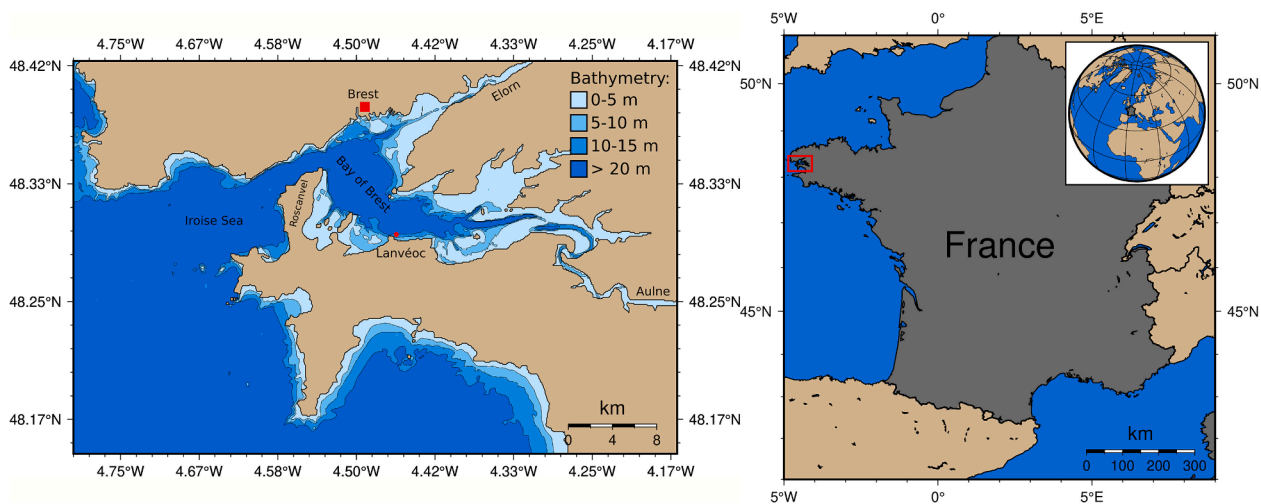
Fig. 1. Map of the Bay of Brest (left panel) with the sampling locality, Lanvéoc (red circle), near to the city of Brest (red square) in northwest France (right panel). (For interpretation of the references to colour in this figure legend, the reader is referred to the web version of this article.)

Table 1
Limit of detection (LOD) and relative standard deviation (RSD) calculated from repeated measurements of the external standard material (NIST SRM 612) for their lithium, molybdenum and barium content via LA-ICP-MS. The USGS MACS-3 reference material served as quality control samples in which the measured values ($\pm 1\sigma$) were compared to known reference values (59.6, 1.21 and 62.9 µg g^{-1} for Ba, Mo and Li, respectively) obtained from the GeoReM database (http://georem.mpch-mainz.gwdg.de/).

Sample ID	Date of collection	Ba/Ca$_{shell}$			Mo/Ca$_{shell}$			Li/Ca$_{shell}$		
		LOD (mmol mol^{-1})	RSD (%)	MACS-3 values (µg g^{-1})	LOD (mmol mol^{-1})	RSD (%)	MACS-3 values (µg g^{-1})	LOD (mmol mol^{-1})	RSD (%)	MACS-3 values (µg g^{-1})
Shell A	30. Aug 11	9×10^{-6}	2	56.6 ± 4.8	2×10^{-5}	4.7	1.5 ± 0.2	3×10^{-3}	3.2	49.9 ± 1.9
Shell B	30. Aug 11	1×10^{-5}	1.7	65.6 ± 4.3	2×10^{-6}	5.7	2.1 ± 0.2	5×10^{-3}	1.9	56.3 ± 1.2
Shell C	30. Aug 11	8×10^{-6}	2.6	54.8 ± 4.6	8×10^{-7}	3.6	1.4 ± 0.3	2×10^{-3}	6.6	52.2 ± 1.6
Shell D	23. Oct 12	9×10^{-6}	5.5	66.9 ± 4.0	8×10^{-7}	7.1	2.1 ± 0.4	4×10^{-3}	5.1	55.5 ± 1.2
Shell E	23. Oct 12	5×10^{-6}	3.1	58.8 ± 2.5	9×10^{-6}	3.8	1.5 ± 0.1	5×10^{-3}	2.7	53.5 ± 1.3
Shell F	23. Oct 12	1×10^{-5}	2.5	66.2 ± 5.8	8×10^{-7}	5	1.7 ± 0.2	4×10^{-3}	2.4	53.8 ± 1.1
Shell G	15. Nov 19	1×10^{-5}	7.1	54.4 ± 2.5	2×10^{-5}	4.2	1.5 ± 0.1	1×10^{-2}	4.9	54.2 ± 1.5
Shell H	15. Nov 19	2×10^{-5}	1.9	58.9 ± 2.2	3×10^{-5}	3	1.6 ± 0.1	1×10^{-2}	1.7	53.5 ± 0.8
Shell I	15. Nov 19	5×10^{-6}	3.4	49.9 ± 3.3	1×10^{-5}	4.5	1.2 ± 0.1	3×10^{-3}	4.2	49.8 ± 1.5

Chemistry (Mainz, Germany). The laser operated in a line scan mode by ablating shell material on the outer shell surface perpendicular to the growth direction and parallel to the striae (Fig. 2). To avoid sample contamination, each scan was pre-ablated with a laser spot size of 100 µm at a constant speed of 80 µm s^{-1}. Then, sample ablation was performed using a laser spot size of 80 µm at a speed of 5 µm s^{-1}. Each line scan attained a total length of 600 µm. Reference materials used for calibration and quality control were analyzed in a similar way. Given the high growth rates in *P. maximus* during the second year of growth (i.e., after the 1st winter growth line), a nearly daily resolution was obtained by sampling every stria from the winter growth mark to the ventral margin. Measured signal intensities were averaged for each line scan as the distribution of trace elements within a single stria was considered to be homogeneous (Barats et al., 2007).

A NewWave Research UP-213 Nd:YAG laser ablation system was used for ablation performing at a repetition rate of 10 Hz with a laser energy density of ca. 15.8 J cm^{-2}. Helium (quality 5.0) served as an initial carrier gas at a flow rate of 0.57 L/min. After ablation, ion intensities were analyzed using a Thermo Fisher Element 2 single collector sector-field ICP-MS, connected to the laser ablation system, with argon (quality 5.0, flow rate 0.77 L min^{-1}) as carrier gas. The synthetic silicate glass, NIST SRM 612, was used as a reference material and served as an external standard (values obtained from the GeoReM database version 29; http://georem.mpch-mainz.gwdg.de/; last access: 2 July 2021; Jochum et al., 2011), and ^{43}Ca was used as an internal standard.

Data reduction was performed according to the calculations provided by Longerich et al. (1996) and Jochum et al. (2011, 2007) using an in-house Microsoft Excel spreadsheet template. Detection limits (LOD) were computed based on the 3σ criterion using the blank signal of each measurement, i.e., 15 s prior to sample ablation. Element-to-calcium ratios were significantly higher than the calculated detection limits for the target analytes (Table 1), with an average LOD of 1×10^{-5} mmol mol^{-1} for Ba, 1×10^{-5} mmol mol^{-1} for Mo and 6×10^{-3} mmol mol^{-1} for Li. Uncertainties of reproducibility were expressed as the relative standard deviation in percent (RSD%) and calculated from repeated NIST SRM 612 measurements. On average, the calculated RSD % was 3.3 % for Ba, 4.6 % for Mo and 3.6 % for lithium. In addition, the synthetic carbonate powder pellet, USGS MACS-3, was used as quality control material and treated as an unknown sample. Table 1 summarizes the blindly measured MACS-3 values with an average 59.1 ± 3.8 µg g^{-1} for Ba (ref. value: 59.6 µg g^{-1}), 1.6 ± 0.2 µg g^{-1} for Mo (ref. value: 1.21 µg g^{-1}) and 53.2 ± 1.3 µg g^{-1} for Li (ref. value: 62.9 µg g^{-1}). Published reference values were obtained from the GeoReM database. Due to heterogeneously sized particles of the MACS-3 carbonate pellet, changes in the ablation behavior potentially led to differences in ionization causing deviations between the published reference values and the blindly measured MACS-3 samples. In addition, uncertainties of the non-certified reference material (Jochum et al., 2019) likely also accounted for observed deviations.
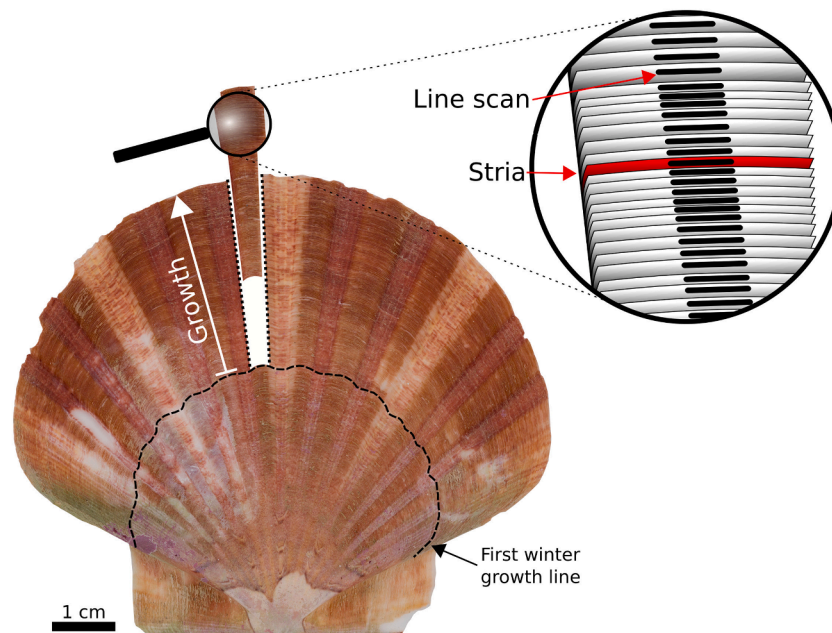
Fig. 2. Left valve of a *P. maximus* specimen and a schematic representation (magnification) of the analyzed shell portion. All shells used in this study experienced one winter growth line (dashed black line). LA–ICP–MS scans were obtained from a shell section covering the portion between the ventral margin and the winter growth line. Each line scan was positioned on a daily increment (stria) perpendicular to the direction of growth.

2.3. Temporal alignment of geochemical information

Shells of *P. maximus* are known to form visible growth increments and lines (aka 'striae') on a daily basis (e.g., Chauvaud et al., 1998; Lorrain et al., 2000). By backdating from the last known increment, i.e., the date of collection corresponding to the last increment visible at the ventral margin, it was possible to place each stria into a precise temporal context (Fig. 2), as long as the shell collection was accomplished during the main growing season. By means of image processing, the clean outer shell surface of each specimen was used for growth pattern analysis. With a Canon EOS 600 DSLR camera connected to a Wild Heerbrugg binocular microscope equipped with a Schott VisiLED MC 1000 light source (sectoral dark field), images were taken along one of the main growth axes between the ventral margin and the first winter line. Obtained, overlapping images were then stitched together using the Image Composite Editor software (version 2.0.3.0; by the Microsoft Research Computational Photography Group). The width of each microgrowth increment was determined by measuring the distance between two adjacent striae and converting the pixel distance into a μm-scale. By including the daily periodicity of striae formation, growth rates were expressed in μm day^{-1}. Since the last formed increments were sometimes hard to identify, because of small fractures at the ventral margin, it was necessary to compare growth patterns of contemporaneous specimens and crossdate the growth curves by minimizing the sum of least squares. As described in previous studies (Thébault et al., 2009, 2006) difficulties in the visual growth increment determination process and subjective inter-reader discrepancies can lead to small uncertainties in the absolute dating of geochemical data and according to the calculations of a previous study (Fröhlich et al., 2022), a small uncertainty of ± 2 days in the temporal alignment of the geochemical data was considered.

2.4. Phytoplankton determination and instrumental data

Phytoplankton data were collected between 13 January and 24 October 2011, between 17 January and 18 December 2012 and between 28 January and 18 December 2019. The sampling frequency in 2011 was twice per week in spring to once per week during the rest of the year,

resulting in a total of 52 samples. In 2012, water samples were collected on a weekly basis in spring and biweekly in summer to winter, providing a total of 26 samples. In 2019, a total of 21 water samples were collected on a biweekly basis. Each water sample was collected using a 5 L Niskin bottle that was placed vertically, ca. 1.5 m below the water surface. For phytoplankton species determination, 250 mL of the water sample was carefully filled into a silicon tube, to avoid turbulence and disintegration of intact phytoplankton cells. The phytoplankton cells were fixed in 2.5 mL Lugol's solution within one hour after sampling and stored at a dark place to avoid UV-damaging. The identification of phytoplankton taxa as well as the calculation of the respective cell concentration were performed using an aliquot of 50 mL of the water sample that was filled into a sedimentation column. After 24 h, the phytoplankton cells settled on a microscope glass slide and the different cells were identified and counted with an inverted microscope (Axio Observer.A1-ZEISS). Due to very small cell sizes and/or only minor differences in cell ornamentations, the assignment to a species-rank was not always unambiguous for some phytoplankton cells. Consequently, these cells were identified according to their phytoplankton genera and/or their cell size. The identification in 2011 and 2012 differed slightly from 2019, e.g., the dinoflagellate genus *Gymnodinium* spp. was subclassed into *Gymnodinium* spp. < 20 μm and > 20 μm in only 2011 and 2012. In the following, the term phytoplankton bloom refers to an ephemeral, relatively large increase or maximum in the observed cell abundance of a given phytoplankton taxa time-series. Chlorophyll *a* and pheophytin pigment concentration were extracted by filtering water samples with glass fiber filters (GF/F Whatman) and adding 6 mL of 90 % acetone. After storing the samples at a dark place for 12 h at 4 °C, each sample was centrifuged (at 3000 rpm for 5 and 10 min) and fluorescence was measured using a Turner Design fluorometer. Finally, pigment concentration were obtained following the calculations provided by Lorenzen (1966).

2.5. Pseudo-random sampling method to detect potential patterns between trace element profiles and phytoplankton taxa

In order to determine potential relationships between the measured trace element profiles and the phytoplankton data, a pseudo-random sampling method was applied. This algorithmic approach (using the

scripting language C++) consisted of multi-step Monte Carlo simulations, where each simulation encompassed 10^7 independent runs (Fig. 3). In total 294 simulations were performed, resulting in 2.94 billion runs. The objective of this method was to identify potential relationships in the patterns of trace element profiles, i.e., the relative timing of transient trace element peaks, and those of phytoplankton data.

In general, each run consisted of seven consecutive steps: (1) Choosing the number of different phytoplankton taxa (i.e., number of individual time-series) that are taken into account in the respective run,

by pseudo-randomly generating a number (z) between 1 and n (number of considered phytoplankton taxa). (2) Randomly select z phytoplankton time-series among the included taxa (Fig. 3A; Supplementary Table 1, 2). (3) Assign a specific time-lag (in days) to each of the selected phytoplankton time-series. This time lag is randomly selected within a predefined range (Fig. 3B). (4) In addition to the temporal lag, a time-series specific weighting factor was randomly assigned to each phytoplankton taxon, where the factor is selected between 0 and 1 (Fig. 3B). (5) Generating a continuous phytoplankton time-series based on the specific temporal shifts and weighting factors, by computing the
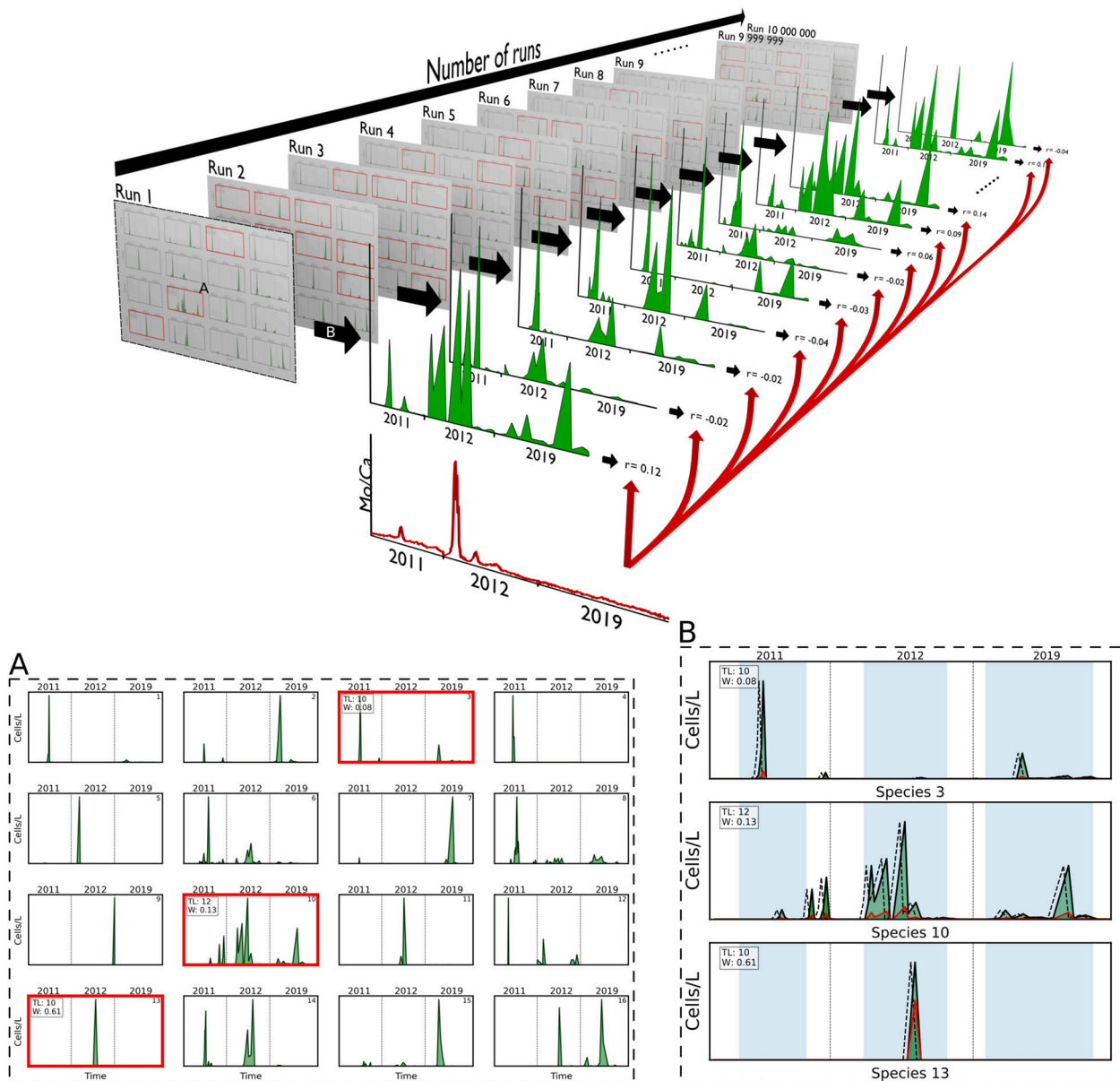

Fig. 3. Simplified schematic representation of the pseudo-random sampling method used in this study. Exemplarily, 16 different phytoplankton taxa time-series from three years (2011, 2012 and 2019) were included and depicted in **A** (each subplot corresponds to the cell concentration time-series data of one phytoplankton taxon). For each run, a random number of phytoplankton time-series was selected, i.e., subplots marked with a red frame. For instance, in the first run (**A**) the three phytoplankton taxa 3, 10 and 13 were selected. In addition, a time lag (in days between a given range; TL) and a weighting factor (between 0 and 1; W) were randomly generated and assigned to each phytoplankton time-series. **B** shows how the individual time-series were processed, i.e., the dashed black line displays the original cell concentration data, the green area represents the temporally shifted time-series and the red graph shows the temporally lagged and weighted phytoplankton time-series. The blue area in **B** delimits the region of interest in the processed phytoplankton time-series that is defined by the date of the first and last trace element measurement within the respective year. As a next step, the selected and modified phytoplankton data were combined into a continuous time-series and the Pearson correlation coefficient between the new phytoplankton time-series and the trace element profile was calculated for each run (*r*). This procedure was repeated iteratively 10^7 times and the best results, according to the Pearson correlation coefficient, were stored. (For interpretation of the references to colour in this figure legend, the reader is referred to the web version of this article.)

weighted and time-lagged sum of the phytoplankton data that are included in the current run. (6) Compare the obtained phytoplankton time-series to the respective trace element profile by calculating the Pearson correlation coefficient (*r*). (7) If the Pearson correlation coefficient of the respective run is larger than that of previous runs, store the selected phytoplankton data including time lags and weighting factors (i.e., the 50 best runs, according to the Pearson correlation coefficient, were stored).

Returning the best out of 10^7 runs, according to the Pearson correlation coefficients obtained from one simulation, provided an estimate of the best possible combination. To account for potential patterns at differently lagged phytoplankton time–series, 25 simulations were performed considering predefined time lags (3 days) between 0 and 50 days, i.e., the first simulation covered 0 to 2 days, the second 2 to 4 days, the third 4 to 6 days, and so forth. In addition, 24 simulations were implemented comprising larger time lags (5 days) between 0 and 50 days, i.e., the first simulation encompassed 0 to 4 days, the second 2 to 6 days, etc. This simulation strategy ensured to cover all potential time lags between 0 and 50 days at various temporal windows. As mentioned in section 2.4, the phytoplankton identification details slightly differed in the three studied years. Therefore, two sets of simulations were performed: The first covered the main phytoplankton data from all three years (Supplementary Table 1) by summarizing individual phytoplankton taxa to phytoplankton groups, e.g., *Gymnodinium* spp. < 20 μm and *Gymnodinium* spp. > 20 μm were combined into one *Gymnodinium* spp. group. This grouping strategy ensured to compare phytoplankton groups from all three years but decreased the number of comparable phytoplankton taxa. Since a more detailed phytoplankton determination was available for 2011 and 2012 (Supplementary Table 2), the second set of simulations was performed solely focusing on these two years, discarding the less detailed phytoplankton identification in 2019. In order to calculate the Pearson correlation between the phytoplankton data and the trace element profiles, the time-series were cut to the time range covered by the trace element data in the corresponding year (Fig. 3B, blue area). To reduce the number of possible combinations and to focus solely on the most dominant taxa, only phytoplankton time-series were included that provided a maximum cell concentration>1000 cells/L in one of the studied years. In total, 47 phytoplankton groups were taken into account in the first set of simulations and 50 groups in the second set (see Supplementary Tables S1 and S2). Unlike Ba/Ca$_{shell}$ and Mo/Ca$_{shell}$ profiles, the Li/Ca$_{shell}$ time-series yielded a growth rate related background signal (Thébault and Chauvaud, 2013) that had to be removed from the Li/Ca$_{shell}$ data to extract transient Li peaks and to normalize the background level. This was accomplished by using the Li/Ca$_{shell}$-to-daily growth rate dependency calculated by Thébault and Chauvaud (2013).

Since no causal relationship could be derived from the purely deterministic calculations, the individual results had to be evaluated separately. To address the quality (i.e., to which extent the temporally shifted and weighted phytoplankton time-series agreed with the trace element profiles) of a simulation at a certain time interval relative to that of other tested time lags, the Pearson correlation coefficients provided a first evaluation. Simulations showing larger correlation coefficients were then manually evaluated by comparing the simulated phytoplankton time-series with the trace element profiles following the premise of a potential relationship. Finally, the hypothetically determined scenarios (or best matching scenarios), i.e., phytoplankton species and time lags used to explain the occurrence of trace element peaks, were contextualized ecologically and interpreted accordingly.

3. Results

3.1. Growth rate and trace element profiles in P. maximus

Although growth rates varied among specimens, especially during the main growing season, the overall growth patterns were largely synchronous among contemporaneous bivalves (Fig. 4). In all three studied years, shell growth commenced in March at growth rates between 20 and 60 μm day^{-1}. In 2011 and 2012 (Fig. 4A, B), the growth rates gradually increased until early May (reaching average growth rates of ca. 200 μm day^{-1}), whereas in 2019 (Fig. 4C), growth rates initially peaked in mid-April (ca. 200 μm day^{-1}) but dropped rapidly until end of April (68 μm day^{-1} on 28 April). After this growth slowdown, the growth rates successively increased reaching maximum values in early August (ca. 280 μm day^{-1}). Similarly, maximum growth in 2011 and 2012 occurred between the end of July and early August with growth rates of ca. 300 μm day^{-1} and 280 μm day^{-1}, respectively. Growth rates started to decline between the end of August and September in all three years.

Trace element profiles of the studied years exhibited a similar pattern among specimens from the same population (Fig. 5). In general, a flat baseline level was episodically interrupted by distinct peaks. Average background levels were 0.60 ± 0.06 μmol mol^{-1} for Ba/Ca$_{shell}$, 0.04 ± 0.01 μmol mol^{-1} for Mo/Ca$_{shell}$ and 33.73 ± 4.19 μmol mol^{-1} for Li/Ca$_{shell}$. In 2011, four large Ba/Ca$_{shell}$ peaks were detected with the highest elevation in early August (1.77 μmol mol^{-1}; Fig. 5A). From all three years, the largest Ba peak values were determined in August 2012 reaching molar ratios of 3.66 μmol mol^{-1} (Fig. 5B). Additionally, three distinct Ba maxima occurred between June and July 2012. In 2019, elevated Ba/Ca$_{shell}$ values (1.63 μmol mol^{-1}) were obtained between early July and August (Fig. 5C). The Mo/Ca$_{shell}$ profiles of 2011 showed only one distinct Mo/Ca$_{shell}$ maximum in late May (0.19 μmol mol^{-1}; Fig. 5D), whereas in 2012, three ephemeral peaks of decreasing magnitudes were measured between April and July with values in the range of 0.08 and 1.07 μmol mol^{-1} (Fig. 5E). No Mo/Ca$_{shell}$ peaks were observed in shells from 2019 (Fig. 5F). The Li/Ca$_{shell}$ profiles of all three years exhibit only one sharp Li/Ca$_{shell}$ peak in mid-June 2011 with an average value of 132.93 μmol mol^{-1}. This large peak was enveloped by smaller Li/Ca$_{shell}$ fluctuations between 38 and 58 μmol mol^{-1}.

3.2. Phytoplankton dynamics in 2011, 2012 and 2019

In 2011, the phytoplankton dynamics (Fig. 6A) showed increasing chlorophyll *a* levels between February (0.67 μg L^{-1}) and early May (5.11 μg L^{-1}) that coincided with the formation of the second largest diatom bloom (up to 742,500 cells L^{-1} on 02 May) in 2011, while pheophytin pigment concentrations were low (between 0.23 and 0.80 μg L^{-1}). Dinoflagellate cell concentration reached its annual maximum of 347,080 cells L^{-1} on 23 May and was accompanied by a peak in pheophytin pigments (1.64 μg L^{-1}). The largest diatom spring bloom occurred on 06 June (4,072,860 cells L^{-1}) with chlorophyll *a* and pheophytin pigment concentration of 3.52 and 1.88 μg L^{-1}, respectively. Until the end of August, neither large diatom nor dinoflagellate blooms developed, as reflected by low levels of chlorophyll *a* fluctuating between 0.97 and 2.19 μg L^{-1}. However, pheophytin concentration consistently showed high values ranging from 1.02 to 1.57 μg L^{-1}. The diatom community was largely dominated by the taxon *Chaetoceros* spp. that made up nearly 80 % of the total diatom cells recorded in 2011 (Fig. 6 A; left panel), followed by *Dactyliosolen fragilissimus* (5.3 %), *Guinardia delicatula* (3.4 %) and *Leptocylindrus danicus* (3.0 %). The dinoflagellates were mainly composed of two taxa, i.e., *Heterocapsa minima* and *Gymnodinium* spp. (size fraction > 20 μm) that accounted for 41.1 % and 39.1 % of the total dinoflagellate cells in 2011.

The phytoplankton dynamics in 2012 (Fig. 6B) differed significantly from that observed in 2011 showing two chlorophyll *a* spring peaks, i.e., on 03 April (4.44 μg L^{-1}) and on 10 May (9.77 μg L^{-1}). The first chlorophyll *a* peak was associated with an early diatom bloom (476,990 cells L^{-1}) which was followed by the first and largest dinoflagellate efflorescence in 2012 on 24 April (253,960 cells L^{-1}). Two large diatom summer blooms occurred on 28 June (1,195,392 cells L^{-1}) and on 24 July (1,395,940 cells L^{-1}) that were preceded by smaller dinoflagellate blooms on 31 May (119,040 cells L^{-1}) and on 06 July (119,680 cells L^{-1}).
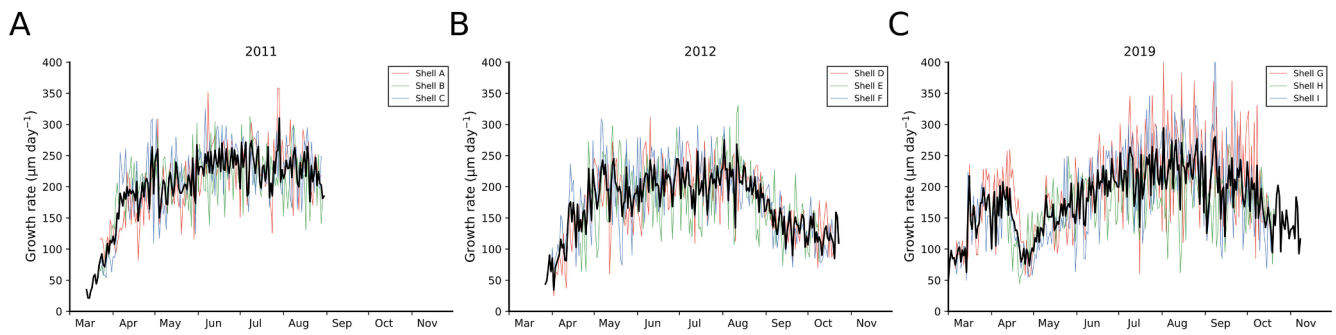
Fig. 4. Growth rates measured from three contemporaneous specimens from 2011 (**A**), 2012 (**B**) and 2019 (**C**). The black line depicts the average growth rate. The last measured growth rate equals to the date of collection of the three individuals in all three years.
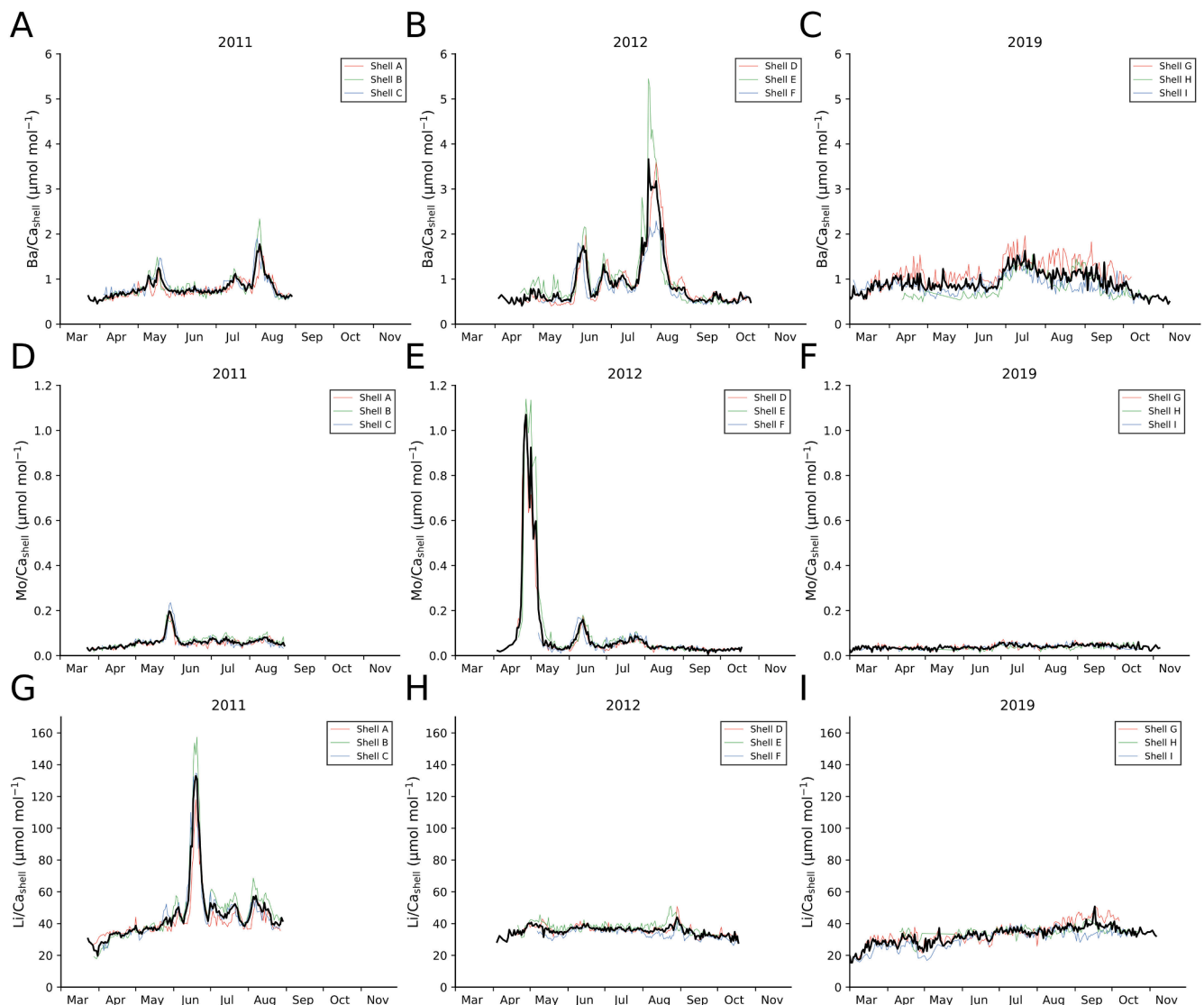

Fig. 5. Trace element profiles (Li/Ca$_{shell}$, Mo/Ca$_{shell}$ and Ba/Ca$_{shell}$) measured in three contemporaneous *P. maximus* specimens from 2011 (**A, D, G**), 2012 (**B, E, H**) and 2019 (**C, F, I**). Average element-to-calcium ratios are indicated as black line.

The summer diatom blooms were related with higher chlorophyll *a* levels between 4.74 and 3.09 µg L^{-1}. The pheophytin pigment concentration roughly followed the chlorophyll *a* pattern with highest concentrations on 26 March (1.55 µg L^{-1}), 10 May (1.40 µg L^{-1}) and 28 June (1.60 µg L^{-1}) followed by lower concentrations throughout the rest of the year (0.62 ± 0.3 µg L^{-1}). Similar to 2011, the majority of diatom cells

belonged to the diatom taxon *Chaetoceros* spp. that accounted for 63.7 % of the total diatom cells. The dinoflagellate community was dominated by cells of the taxon *Gymnodinium* spp. (size fraction < 20 µm; 50.8 %) and *Heterocapsa minima* (27.6 %).

In 2019, the phytoplankton dynamics (Fig. 6C) was characterized by two chlorophyll *a* maxima in spring, i.e., on 19 March and 30 April with
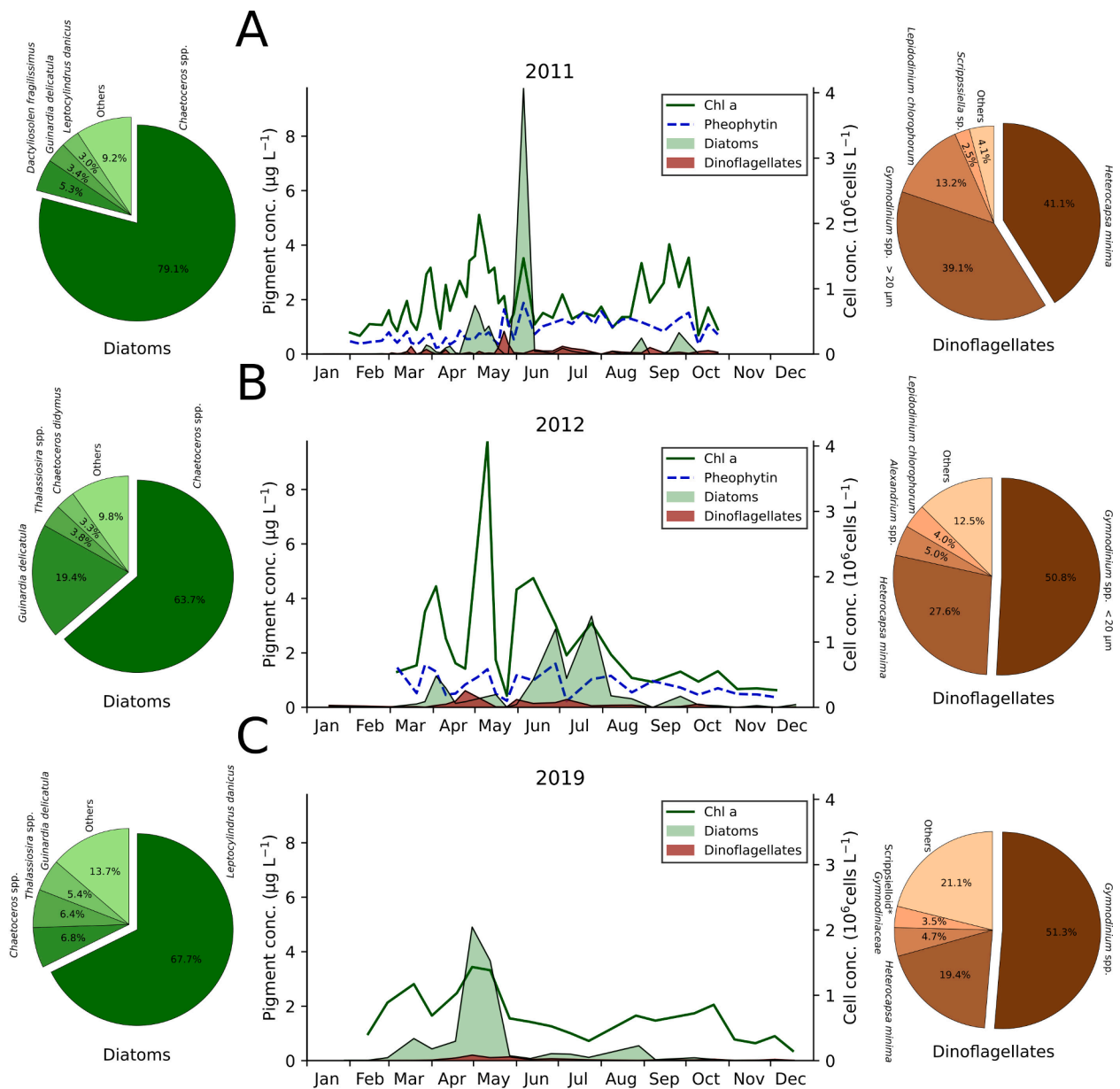
Fig. 6. Overview of the phytoplankton dynamics observed in the Bay of Brest (Lanvéoc) in 2011 (**A**), 2012 (**B**) and 2019 (**C**). Pigment concentrations represented as solid green and dashed blue lines, i.e., chlorophyll *a* and pheophytin (in 2011 and 2012), respectively. Pie charts display the diatom (left panel) and dinoflagellate (right panel) community composition, according to their relative abundance, observed in the respective years (* dinoflagellate group that comprises cells of *Scrippsiella* spp., *Pentapharsodinium* spp. and *Ensiculifera* spp.). (For interpretation of the references to colour in this figure legend, the reader is referred to the web version of this article.)

concentrations of 2.81 and 3.44 μg L^{-1}, respectively. These peaks in chlorophyll *a* pigments coincided with two diatom blooms. The first yet small spring bloom occurred on 19 March with cell concentrations reaching 338,340 cells L^{-1} and the second or the largest bloom emerged on 30 April with 2,044,640 cells L^{-1}. A dinoflagellate effflorescence developed (reaching 83,680 cells L^{-1}) contemporaneously to the late diatom spring bloom (30 April). During summer, chlorophyll concentrations remained low (between 0.72 and 1.65 μg L^{-1}) and only smaller diatom blooms evolved with cell concentrations below 228,060 cells L^{-1} (on 28 August). Furthermore, no dinoflagellate blooms were recorded during summer. Unfortunately, pheophytin pigment concentrations were not recorded in 2019. Unlike 2011 and 2012, the dominant diatom species belonged to *Leptocylindrus danicus* that made up 67.7 % of the total diatom cells, followed by *Chaetoceros* spp. (6.8 %). Similar to 2011 and 2012, the dinoflagellate taxa *Gymnodinium* spp. (51.3 %) and

Heterocapsa minima (19.4 %) formed the predominant dinoflagellate groups observed in 2019.

3.3. Pseudo-random sampling method results

The simulations used to derive potential patterns that could explain the formation of Ba/Ca$_{shell}$ peaks resulted in Pearson correlation coefficients between 0.67 and 0.90 ($p < 0.05$), with three local maxima of gradually decreasing coefficients at time lags of 8 to 12, 24 to 28 and 36 to 40 days, respectively (Fig. 7A, B). Evaluating the generated time-series (temporally lagged and weighted combination of phytoplankton taxa) for these intervals demonstrate that the best agreement to the Ba/Ca$_{shell}$ profiles was obtained for a scenario with a time lag of 8 to 12 days (Fig. 7A, B; subplots). At this time lag, the scenario considering a 5-day interval (Set 2) revealed the strongest similarity with the Ba/Ca$_{shell}$
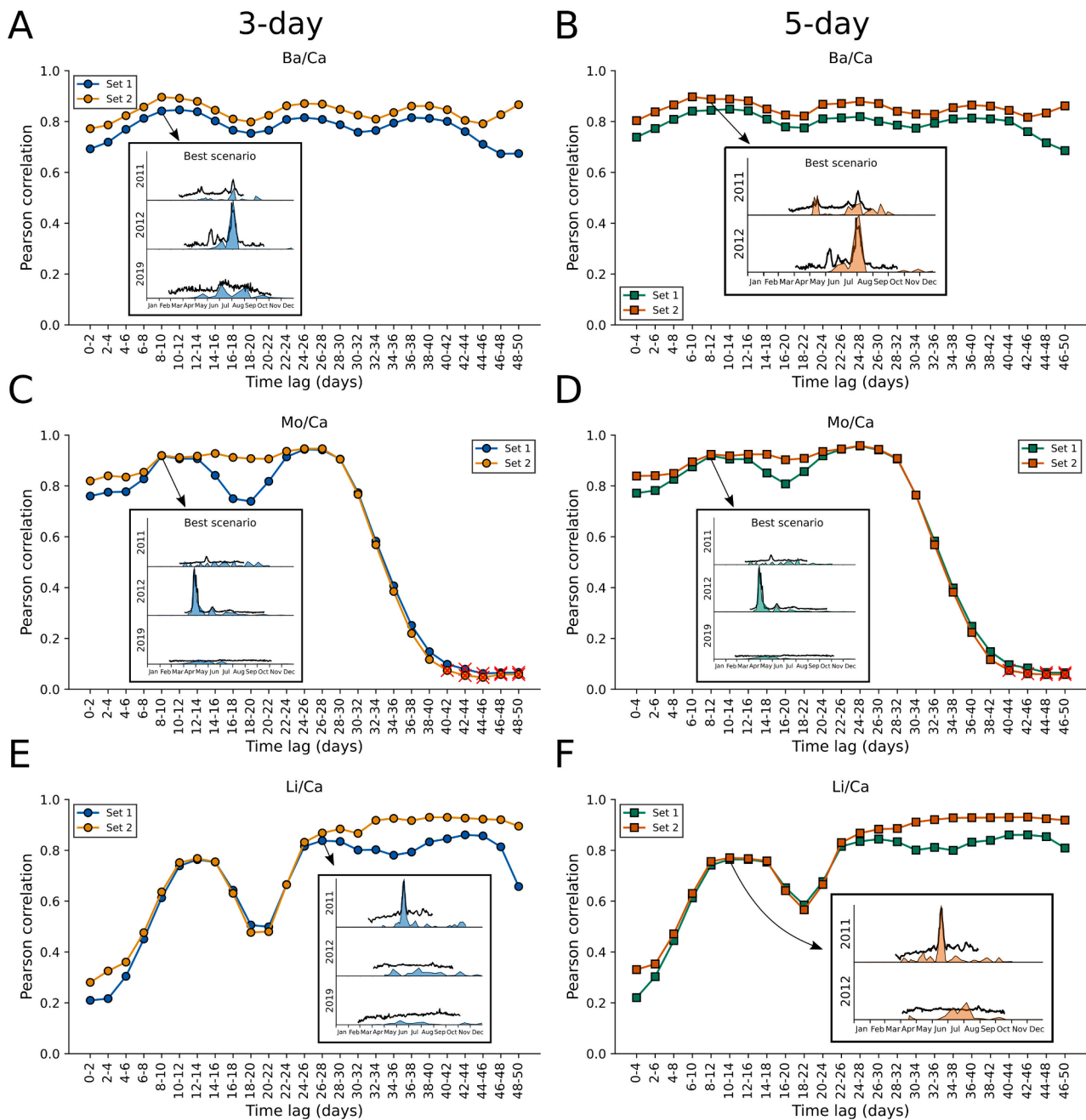
Fig. 7. Pearson correlation results obtained from the pseudo-random sampling method applied on the various phytoplankton time-series versus Ba/Ca$_{shell}$ (**A, B**), Mo/Ca$_{shell}$ (**C, D**) and Li/Ca$_{shell}$ profiles (**E, F**) at different temporal windows (see section 2.5). Correlations that were statistically not significant were indicated with a red cross (**C, D**). Plots on the left side show results for the simulated time interval of 3 days and on the right the results for a 5-day interval. Set 1 simulations include lower resolved phytoplankton taxa but were applied to three different years, while set 2 simulations include higher resolved phytoplankton groups but were confined to 2011 and 2012. Small graphs in each subplot depict the best hypothetical scenario obtained, i.e., the temporally shifted and weighted phytoplankton time-series that fitted best to the magnitude and timing of trace element peaks. Results of all simulation are illustrated in the supplementary materials. Since only one large Li/Ca$_{shell}$ peak (in 2011) was observed in the studied years, a single best phytoplankton pattern could not be established. Instead, several scenarios at different time lags provide a good agreement with the Li/Ca$_{shell}$ profiles (see section 4.3). (For interpretation of the references to colour in this figure legend, the reader is referred to the web version of this article.)

peaks, i.e., all distinct peaks matched with a phytoplankton bloom except for the first Ba/Ca$_{shell}$ peak in 2012 (Fig. 7B). Results obtained for other simulations (Supplementary Figs. S1 to S4) indicate that neither larger or shorter time lags resulted in a sufficiently strong correlation with the trace element profiles. For most of these scenarios, peaks in the phytoplankton data show no consistent pattern with the Ba/Ca$_{shell}$ profiles. The simulations analyzing the time lag between 8 and 12 days revealed a compelling pattern for the diatom species *Thalassionema*

nitzschioides with the timing of Ba/Ca$_{shell}$ peaks, i.e., blooms of this diatom taxon coincided with the formation of Ba enrichments in the shell calcite in all three years. In addition, the non-toxic dinoflagellate species *Lepidodinium chlorophorum* and other diatom groups (different species of the genus *Chaetoceros* (*C. socialis*, *C. debilis* and *C. danicus*) as well as aggregated cells of this taxon (*Chaetoceros* spp. chains) and the diatom *Cerataulina pelagica*) also coincided with the timing of subsequent Ba/Ca$_{shell}$ peaks at time lags between 8 and 12 days, but were

confined to one or two of the studied years.

Simulations evaluating phytoplankton patterns in relation to Mo/Ca$_{shell}$ profiles (Fig. 7C, D) showed a large variability in the Pearson correlation coefficients at different time lags that ranged between 0.05 (statistically not significant; $p > 0.05$) to 0.96 ($p < 0.05$). Correlation coefficients dropped gradually at time intervals>30 days. Although high Pearson correlation coefficients were calculated for time lags of 24 to 28 days, the resulting phytoplankton combinations failed to provide a pattern analogous to the Mo/Ca$_{shell}$ profiles. For instance, the second and third Mo/Ca$_{shell}$ peak in 2012 could not be wiggle–matched to corresponding phytoplankton blooms (Supplementary Figs. S5 to S8). However, the phytoplankton pattern that was detected for an 8-to-12-day time lag strongly agreed with the measured Mo/Ca$_{shell}$ peaks in 2012 (subplots in Fig. 7C, D). The respective simulations revealed that the shell Mo profiles coincided with the timing of two dinoflagellate genera, i.e., *Gymnodinium* spp. and *Prorocentrum* spp. (including *P. minimum*, *P. cordatum* and *P. balticum*). In particular, time-series of the small dinoflagellate *Gymnodinium* spp. ($<20 \, \mu$m) and *P. balticum* showed a high degree of similarity with the Mo/Ca$_{shell}$ profiles, according to simulations of set 2 with higher taxonomic phytoplankton resolution.

The Pearson correlation coefficients calculated from the simulations on Li/Ca$_{shell}$ at different time lags (Fig. 7E, F) exhibited values between 0.21 and 0.93 ($p < 0.05$). The first correlation maximum was observed at a time lag of 10 to 14 days (see subplot in Fig. 7F). The high level of synchronicity at this time interval was induced by matching the largest diatom bloom that emerged in all three years (*Chaetoceros* spp.) with the large Li/Ca$_{shell}$ peak in 2011. However, this phytoplankton configuration did not agree well to the Li/Ca$_{shell}$ profile observed in 2012 as well as to the smaller Li/Ca$_{shell}$ peaks observed in 2011. Apart from this, results obtained for larger time lags (Supplementary Figs. S9 to S12) exhibited high Pearson correlation coefficients with scenarios that fit well to the Li/Ca$_{shell}$ profiles (e.g., subplot in Fig. 7E). Accordingly, a best matching scenario could not be determined. This difficulty occurred because only one prominent Li/Ca$_{shell}$ peak was measured within the studied years, which complicated the detection of potential patterns. Instead, several phytoplankton blooms at different time lags fitted to the trace element peak resulting in larger correlation coefficients.

4. Discussion

The timing as well as the magnitude of transient trace element peaks in profiles of *P. maximus* shells from 2011, 2012 and 2019 exhibited striking similarities among individuals from the same population, confirming previous studies according to which the formation of Ba/Ca$_{shell}$, Mo/Ca$_{shell}$ and Li/Ca$_{shell}$ enrichments in bivalve shells is environmentally driven (e.g., Barats et al., 2010; Gillikin et al., 2008; Thébault et al., 2009; Thébault and Chauvaud, 2013). The results obtained from the pseudo-random sampling simulations cast new light on the relationship between such trace element peaks and the phytoplankton dynamics that prevailed during shell growth. For all three elements analyzed in this study, a potential explanation could be derived by considering a short time lag of 8 to 12 days between phytoplankton events and trace element peaks in the shell. Ba/Ca$_{shell}$ profiles are likely related to the blooms of diatoms, dinoflagellates and flagellates, whereas Mo/Ca$_{shell}$ patterns may reflect blooms of specific nitrate assimilating dinoflagellates. Mo/Ca$_{shell}$ profiles may also potentially be linked to the timing of diatom aggregates in the water column. Li/Ca$_{shell}$ peaks exhibited patterns similar to the blooms of diatoms that produce neurotoxins under stressful environmental conditions as well as large diatom blooms. Accordingly, shell Ba, Mo and Li profiles could be used as valuable chemical proxies to assess past phytoplankton dynamics.

4.1. Phytoplankton and Ba/Ca$_{shell}$ peaks

The high degree of inter-specimen synchronicity of Ba/Ca$_{shell}$ peaks (Fig. 5A, B, C) strongly suggests that common environmental drivers

regulate the timing of enhanced Ba incorporation into the shell carbonate (Barats et al., 2009; Gillikin et al., 2008; Hatch et al., 2013; Marali et al., 2017; Stecher et al., 1996; Thébault et al., 2009; Vander Putten et al., 2000). Several studies put forward a possible correlation between chlorophyll *a* and Ba/Ca$_{shell}$ profiles in bivalve shells (e.g., Doré et al., 2020; Hatch et al., 2013), however, such a linkage could not be established for the studied years 2011 and 2012 in shells of *P. maximus* (Fröhlich et al., 2022). In addition to these years, chlorophyll *a* concentration in 2019 (Fig. 6C) showed no running similarity with the Ba/Ca$_{shell}$ profiles (Fig. 5C) observed in shells from the same year, i.e., the spring bloom related chlorophyll *a* maximum occurred in late April, whereas elevated Ba/Ca$_{shell}$ concentrations appeared in late July to August. This further underscores the limitation of Ba/Ca$_{shell}$ as an indicator of bulk phytoplankton biomass in the ambient water. Likewise, the lack of similarity between total diatom and dinoflagellate cell concentrations and measured Ba/Ca$_{shell}$ profiles in all three years indicates that Ba/Ca$_{shell}$ may not be used as a reliable proxy for bulk diatoms or dinoflagellates in the water column.

It has been proposed that the intake of Ba-rich phytoplankton cells (e.g., diatoms) drives the formation of Ba/Ca$_{shell}$ peaks in the scallop *Comptopallium radula* (Thébault et al., 2009). However, the results obtained from the pseudo-random sampling method indicated no correlation with only a single diatom or dinoflagellate species existed in the studied years. Consequently, Ba/Ca$_{shell}$ peaks could either have a plurispecific cause or are entirely unrelated to the phytoplankton species analyzed in this study. The variable cell-associated Ba concentration reported for various phytoplankton species (Fisher et al., 1991; Martin and Knauer, 1973; Roth and Riley, 1971) supports the notion that different taxa might contribute differently to the formation of Ba/Ca$_{shell}$ peaks (Fröhlich et al., 2022). Moreover, testing potential scenarios of species-specifically weighted time-series at different time lags provide further insights into this relationship between phytoplankton and the formation of Ba/Ca$_{shell}$ peaks. Firstly, phytoplankton time-series did not adequately match the Ba/Ca$_{shell}$ profiles when only a short temporal offset (i.e., 0–2 days and 0–4 days) was considered, as shown by the relatively low Pearson correlation coefficients (Fig. 7A, B). Secondly, the best fitting scenario was obtained for a time lag 8 to 12 days, suggesting that Ba could be incorporated into the shell calcite with a delay of 8 to 12 days after a bloom of Ba-rich phytoplankton. In that scenario (subplot in Fig. 7B), each Ba/Ca$_{shell}$ peak coincided with a phytoplankton bloom, except the first peak in 2012. Although the simulations covering 3-day intervals showed high correlation coefficients at that time lag (Fig. 7 A), the best phytoplankton combination was obtained using a 5-day interval (larger degree of freedom compared to a 3-day interval; Fig. 7B). Accordingly, time lags hypothetically vary between phytoplankton species by more than about 3 days, which would agree with the time lag of 8 to 12 days. However, it remains to be determined if species-specific differences in sinking velocities (e.g., Alldredge and Gotschalk, 1989; Bienfang et al., 1982; Peperzak et al., 2003) and/or a species-dependent variability in the desorption rate of Ba in the digestive tract of bivalves account for the small variance in the estimated time lags.

Evaluating the phytoplankton species obtained from the simulations covering the best fitting time interval, i.e., 8 to 12 days, demonstrates that the diatom species *T. nitzschioides* shares a striking pattern with the Ba/Ca$_{shell}$ profiles. In all three years, the bloom of this taxon coincided with a Ba/Ca$_{shell}$ maximum after shifting the time-series about 10 days (Fig. 8). Blooms of other diatom taxa match with Ba enrichments after similar time lags (e.g., species of the genus *Chaetoceros*) but were confined to one or two of the studied years (Fig. 8). Furthermore, blooms of the dinoflagellate species *L. chlorophorum* are consistent with the timing of Ba/Ca$_{shell}$ peaks in 2011 and 2012 (Fig. 8), suggesting that Ba could also originate from dinoflagellates contributing to the observed Ba/Ca$_{shell}$ peaks in addition to diatoms. This conclusion is supported by the findings of Fisher et al. (1991) showing that dinoflagellates accumulate Ba at high concentrations, and Hatch et al. (2013) who observed a dinoflagellate bloom (*Lingulodinium polyedrum*) several days prior to a
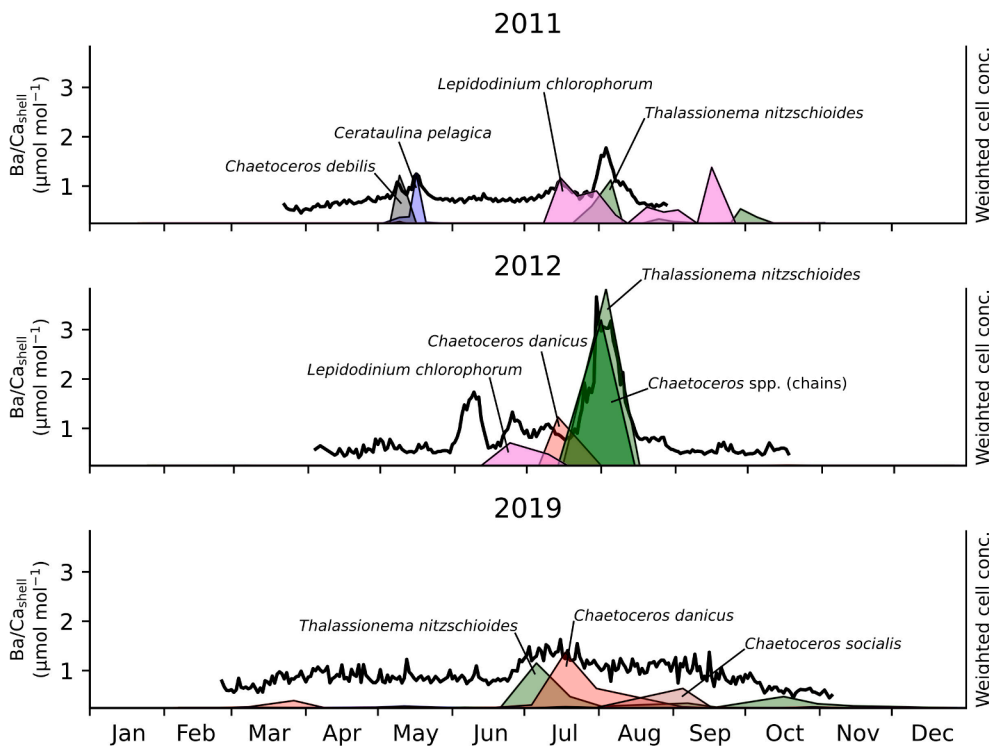
Fig. 8. Ba/Ca$_{shell}$ profiles of 2011, 2012 and 2019 in relation to blooms of diatoms and dinoflagellates that coincide with Ba/Ca$_{shell}$ peaks after applying a time lag between 8 and 12 days, as provided from the pseudo-random sampling simulations. Weighted cell concentration data are given in arbitrary units. Similar species-specific weighting factors were used in each year. The first Ba/Ca$_{shell}$ peak in 2012, which did not match with a diatom or dinoflagellate bloom, agreed well with the timing of a large flagellate bloom (see Supplementary Fig. S13).

Ba/Ca$_{shell}$ peak in the bivalve *Donax gouldii*. However, not every Ba/Ca$_{shell}$ peak coincided with a phytoplankton group considered in these simulations, i.e., the first peak in early June 2012 did not match with a diatom or dinoflagellate bloom (Fig. 8). Despite the lack of similarity between chlorophyll *a* levels and Ba/Ca$_{shell}$ profiles (Fröhlich et al., 2022) as well as their limited capability to reliably reconstruct phytoplankton biomass (e.g., Desortová, 1981; Kruskopf and Flynn, 2006), the first Ba/Ca$_{shell}$ peak in 2012 coincided with the second chlorophyll *a* maximum observed in that year (Fig. 6B), which was associated with a large flagellate bloom (see Supplementary Fig. S13). Accordingly, a link between large flagellate blooms and distinct Ba/Ca$_{shell}$ peaks could be hypothesized (as flagellates were not taxonomically identified in detail, no species-specific flagellate-to-Ba relationship could be established). This assumption is supported by the findings of Fisher et al. (1991) showing that flagellates are associated with large quantities of cell-associated Ba. Therefore, it is likely that in addition to diatoms and dinoflagellates, the ingestion of Ba-enriched flagellates contributed to the formation of Ba/Ca$_{shell}$ peaks in *P. maximus*. The pseudo-random sampling results further strengthened the hypothesis of Ba/Ca$_{shell}$ peaks having a dietary origin, because a potential pattern between the occurrence of various phytoplankton species and the formation of Ba/Ca$_{shell}$ peaks was revealed when a temporal offset between one and two weeks was considered.

4.2. Phytoplankton and Mo/Ca$_{shell}$ peaks

The transient Mo/Ca$_{shell}$ peaks differ significantly in their timing and magnitude between the studied years indicating that the formation of Mo/Ca$_{shell}$ peaks is likely caused by annually changing environmental factors, most likely originating from a dietary source (Tabouret et al., 2012; Thébault et al., 2009). The pseudo-random sampling simulations revealed a phytoplankton scenario for a time lag of 8 to 12 days (similar to that obtained for Ba/Ca$_{shell}$) showing a striking similarity with the Mo/Ca$_{shell}$ profiles. In that scenario, blooms of two dinoflagellate genera (*Gymnodinium* spp. and *Prorocentrum* spp.) agreed well with the occurrence of transient Mo/Ca$_{shell}$ peaks. Especially, the time-series of the dominant dinoflagellate *Gymnodinium* spp. shared a similar pattern with

the Mo/Ca$_{shell}$ profiles in 2012 with three successively decreasing Mo/Ca$_{shell}$ peaks coinciding with three blooms of decreasing cell concentrations (Fig. 9). However, only the size fraction including cells smaller than 20 μm shared this clear pattern with the Mo/Ca$_{shell}$ profiles. In 2011, exclusively cells of *Gymnodinium* spp. larger 20 μm were observed. Interestingly, shifting this time-series (*Gymnodinium* spp. > 20 μm) about the same time lag as *Gymnodinium* spp. < 20 μm from 2012, shows that the Mo/Ca$_{shell}$ peak in 2011 match with one of the recorded *Gymnodinium* spp. blooms (i.e., the sixth bloom in 2011; Fig. 9). Since individual phytoplankton blooms are mostly monospecific (largely dominated by a single phytoplankton taxon), it can be hypothesized that this specific bloom was composed of a smaller *Gymnodinium* species whose cell size fits within the range potentially ingested by *P. maximus*. Conversely, scallops likely filtered out the larger fraction of *Gymnodinium* cells, as particle size is known to be one of the key factors controlling the retention and uptake of phytoplankton cells in scallops (e.g., Beninger et al., 2004; Shumway et al., 1997). In addition to the timing, the magnitude of Mo/Ca$_{shell}$ peaks seems to be resembled by the dinoflagellate cell concentration, except a small deviation of the second Mo/Ca$_{shell}$ peak in 2012. Given the similarity between the *Gymnodinium* spp. time-series and the measured Mo/Ca$_{shell}$ profiles in 2011 and 2012 (Fig. 9), a potential link between this dinoflagellate and the development of Mo/Ca$_{shell}$ peaks can be hypothesized. In 2019, no Mo/Ca$_{shell}$ peak was measured although two *Gymnodinium* spp. blooms were monitored. On the one hand, these blooms coincided with a period of significant shell growth retardation (Fig. 9). On the other hand, no size classification was made for this dinoflagellate in 2019. Consequently, it is difficult to determine if the absence of a Mo/Ca$_{shell}$ maximum is induced by large (>20 μm), non-ingestible *Gymnodinium* spp. cells (similar to the blooms monitored in 2011; Fig. 9) and/or by the strong growth rate reduction that is associated with a restricted food intake (Chauvaud et al., 1998; Lorrain et al., 2000).

A possible mechanism for the observed relationship between *Gymnodinium* spp. blooms and the formation of Mo/Ca$_{shell}$ enrichments is the nitrate assimilation strategy of phytoplankton that requires the presence of Mo which is a crucial constituent of the enzyme nitrate reductase (Collier, 1985; Marino et al., 2003). In marine organisms, ammonium is
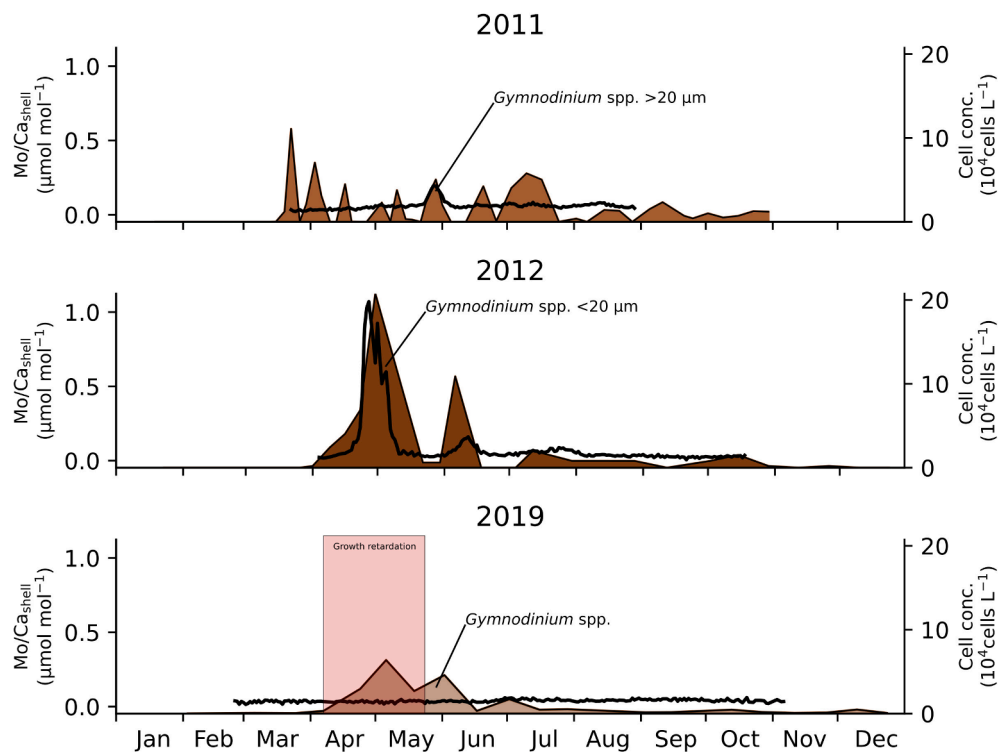
Fig. 9. Mo/Ca$_{shell}$ profiles of 2011, 2012 and 2019 and the cell concentration time-series of the dinoflagellate *Gymnodinium* spp. at different cell size fractions. Dinoflagellate time-series were temporally shifted about 8 days. Red area depicts the period of large growth rate retardation in *P. maximus* observed in spring 2019. (For interpretation of the references to colour in this figure legend, the reader is referred to the web version of this article.)

preferentially used instead of nitrate for nitrogen assimilation (Eppley et al., 1969; Morris and Syrett, 1963) which does not require the activity of Mo-containing nitrate reductase. In turn, periods of low ammonium were shown to be associated with nitrate reductase synthesis in phytoplankton (Eppley et al., 1969; Eppley and Coatsworth, 1968), suggesting a potential relationship between phytoplankton cells grown on nitrates and enhanced Mo incorporation into the shell (Thébault et al., 2009). Accordingly, Mo/Ca$_{shell}$ peaks would resemble the timing and magnitude of large phytoplankton blooms grown on nitrates. Yet, this assumption could not be substantiated in this study, because the large Mo/Ca$_{shell}$ peak in 2011 coincided with a peak in ammonium (see Supplementary Fig. S14). However, minor fluctuations in the Mo/Ca$_{shell}$ profile from 2011 (in June, July and August) seem to be inversely correlated to measured ammonium concentrations (see Supplementary Fig. S14). Unfortunately, ammonium concentrations were not recorded in 2012. Nevertheless, it was demonstrated that some dinoflagellates utilize nitrate instead of ammonium, even when ammonium levels were not limited (Harrison, 1973). Moreover, Yamamoto et al. (2004) showed the affinity of the *Gymnodinium* species *G. catenatum* to assimilate nitrate instead of ammonium, which in turn, requires the presence of nitrate reductase, leading to a high amount of enzyme associated Mo in the dinoflagellate cell. In addition, Ho et al. (2003) observed a 5.6 times higher cellular concentration of Mo in cells of *G. chlorophorum* (13 mmol L^{-1}) compared to other marine phytoplankton taxa reported in that study (2.3 mmol L^{-1}). These findings support the assumption that the ingestion of Mo-rich *Gymnodinium* spp. cells could be linked to the formation of Mo/Ca$_{shell}$ peaks in scallop shells.

In addition to the hypothesis stated previously, Thébault et al. (2022) demonstrated a potential link between the development of diatom aggregates in the water column, especially after large diatom blooms that exhausted nutrient stocks (i.e., silicates), and the formation of Mo/Ca$_{shell}$ peaks in *P. maximus*. These aggregates likely sequester dissolved Mo from the ambient water and lead to the accumulation of Mo in the shell calcite after being ingested by the bivalve. This provides a suitable

explanation for the single Mo/Ca$_{shell}$ peak observed in 2011 (Fig. 5D) that occurred after a large diatom spring bloom when low nutrient conditions and cell collision rates potentially favored the diatom cells to flocculate (Corzo et al., 2000; Thornton, 2002). Likewise, the first diatom spring bloom in 2012 (end of March; Fig. 6B) developed under low silicate conditions (i.e., below the half–saturation constant (K_m) for silicates around 2 μmol L^{-1}; see Supplementary Fig. S15) which potentially led to the formation of aggregates in early 2012 and thus to an enhanced incorporation of Mo into the shell. Accordingly, the development of the first and largest Mo/Ca$_{shell}$ peak in 2012 supports the diatom-aggregate-hypothesis. In 2019, the diatom bloom in early May (Fig. 6C) was dominated by the diatom taxa *Chaetoceros* and *Leptocylindrus* which are known to form aggregates (e.g., Bienfang, 1981; Nashad et al., 2017; Thornton, 2002) when growing under nutrient limitations. However, silicate concentrations only reached low levels approx. two weeks after that diatom bloom (see Supplementary Fig. S15) suggesting no aggregates developed in 2019 and consequently no Mo/Ca$_{shell}$ peak formed.

Both hypotheses, i.e., the link between Mo/Ca$_{shell}$ peaks and blooms of smaller dinoflagellates species of *Gymnodinium* spp. or, alternatively, the formation of diatom aggregates, provide potential pathways explaining the Mo entrainment into the shell material. Moreover, the observation by Thébault et al. (2022) and the results of this study, showing that Mo/Ca$_{shell}$ maxima coincide with a preceding reduction in growth rate of the bivalve (Fig. 4), are consistent with and support both assumptions. On the one hand, blooms of *Gymnodinium* spp. are known to be toxic and negatively affect growth rates in bivalves (Chauvaud et al., 2001, 1998; Widdows et al., 1979). On the other hand, the sedimentation of aggregates can disturb shell growth caused by oxygen depletion and/or gill clogging (Lorrain et al., 2000). Thus, it is likely that the timing and magnitude of Mo/Ca$_{shell}$ peaks record potential changes in phytoplankton dynamics either in the form of large dinoflagellate blooms and/or periods of large diatom blooms coupled to stressful nutrient conditions, which makes Mo/Ca$_{shell}$ a valuable proxy for

ecological reconstructions.

4.3. Phytoplankton and Li/Ca_{shell} peaks

In contrast to Ba/Ca_{shell} and Mo/Ca_{shell} profiles, the only major Li/Ca_{shell} peak occurred in 2011 (Fig. 5G) and no distinct peak was observed in shells from 2012 and 2019 (Fig. 5H, I). This made it difficult to detect potential patterns between trace element profiles and phytoplankton dynamics from different years. Simulating phytoplankton scenarios that can potentially describe the measured Li/Ca_{shell} profiles in all three years suggested an immediate relationship between the timing of a phytoplankton bloom and the formation of Li/Ca_{shell} peaks to be unlikely, as shown by the low Pearson correlation coefficients at small time intervals (0 to 4 days; Fig. 7E, F). For scenarios deduced from simulations considering larger time intervals (>14 days), no suitable pathway could be derived that provides an appropriate ecological interpretation to explain the Li/Ca_{shell} profiles. However, the simulations returned a relatively high correlation with the Li/Ca_{shell} profiles when shifting the most dominant diatom taxon *Chaetoceros* spp. about 10 to 14 days (subplot in Fig. 7F). This observation is in agreement with the findings of Thébault et al. (2022) suggesting that the mass occurrence of diatoms about two weeks earlier could be associated with diatom frustules enriched in Li, similar to Ba (Sternberg et al., 2005). Thus, the frustules transport large quantities of this trace element to the sediment water interface where it is taken up by the scallops. Unlike 2011, no Li/Ca_{shell} peaks were formed in 2012 and 2019 following blooms of the main diatom genus *Chaetoceros*, possibly as a result of much lower cell concentrations.

Evaluating other hypothetical scenarios obtained from the pseudo-random sampling simulations revealed another phytoplankton pattern that match the Li/Ca_{shell} profiles. For shorter time intervals (4–6, 6–8, 8–10 days) the best fitting time-series is obtained for the diatom species *Pseudo–nitzschia pungens* that shares an appealing resemblance to the Li/Ca_{shell} profile in 2011. In fact, performing the pseudo–random

simulations for a time lag of 8 to 12 days but excluding the *Chaetoceros* spp. time-series revealed *P. pungens* to match best with the Li/Ca_{shell} profile, although the correlation metrics was slightly lower. The lower Pearson correlation coefficients can be explained by the first *P. pungens* bloom as well as the bloom in 2012 that do not coincide with a Li/Ca_{shell} peak in 2011, when shifting about 8 to 12 days (Fig. 10). However, the second, third and fourth bloom match with the timing of Li/Ca_{shell} maxima (Fig. 10). The link between blooms of *Pseudo–nitzschia* and Li/Ca_{shell} peaks in scallop shells was already proposed by Thébault and Chauvaud (2013). It was hypothesized that the synthesis of domoic acid (DA), a potent neurotoxin produced by *Pseudo-nitzschia* (Bates et al., 1989), demands the presence of Li (Subba Rao et al., 1998) and lead to the formation of Li/Ca_{shell} peaks after ingestion (Thébault and Chauvaud, 2013). Since the sampling site of phytoplankton and scallops were different in that study (Thébault and Chauvaud, 2013), it was difficult to establish a reliable relationship between the timing and magnitude of blooms and Li/Ca_{shell} peaks due to the spatial variability of *Pseudo–nitzschia*. The present study shows the similarity between the timing of *P. pungens* blooms and Li/Ca_{shell} peaks observed for 2011 supporting the hypothesis by Thébault and Chauvaud (2013). Furthermore, other species of this diatom genus could also produce DA (Bates et al., 2018), suggesting that not only *P. pungens* but also other taxa such as *P. seriata* can potentially contribute to the formation of Li/Ca_{shell} peaks. Indeed, the small Li/Ca_{shell} peaks in July 2011 match with the bloom of *P. seriata* when shifting the time-series about 8 to 12 days (Fig. 10). Yet, a discrepancy is obtained for the year 2012 that experienced blooms of *P. pungens* and *P. seriata* while no Li/Ca_{shell} peaks were measured (Fig. 10). A possible explanation for this inconsistency is that DA is synthesized only when the diatoms are stressed, i.e., by nutrient limitation (Pan et al., 1996) and/or by enhanced grazing activity of zooplankton (Bates et al., 2018). Interestingly, when considering a time lag of 8 to 12 days, the Li/Ca_{shell} peaks in 2011 coincide with periods of high pheophytin levels (an approximation of grazing activity; Chauvaud et al., 2000; Lorenzen, 1967; Strom, 1993) and low levels of silicate, i.e.,
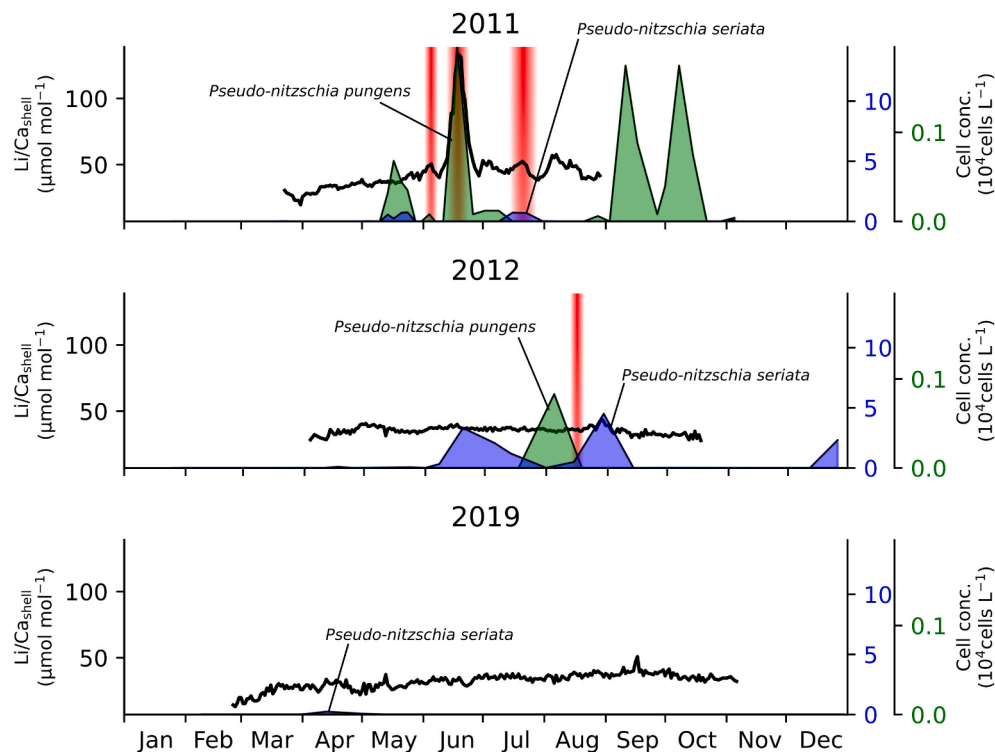

Fig. 10. Li/Ca_{shell} profiles of 2011, 2012 and 2019 and the timing and magnitude of *Pseudo-nitzschia pungens* and *P. seriata* blooms after a short time lag of 8 to 12 days. Red vertical bars indicate periods of stressful conditions (temporally shifted about 12 days), i.e., nutrient limitation and high grazing activity of zooplankton. (For interpretation of the references to colour in this figure legend, the reader is referred to the web version of this article.)

stressful conditions for *Pseudo–nitzschia* cells (Fig. 10; Supplementary Fig. S15; red vertical bars). *Pseudo–nitzschia* blooms that could not be associated with the formation of subsequent Li/Ca$_{shell}$ peaks developed under non-stressful conditions, especially in 2012 when these conditions solely occurred between two successive blooms of *Pseudo–nitzschia* (Fig. 10). These findings support the assumption that the formation of Li/Ca$_{shell}$ peaks could be related to blooms of *Pseudo–nitzschia* but only under certain environmental conditions that triggers the formation of DA. In addition to *Pseudo–nitzschia* species, a potential influence of the benthic diatom *Nitzschia* spp. on the development of Li/Ca$_{shell}$ peaks should be considered in future studies, as this diatom is known to produce DA similar to *Pseudo–nitzschia*.

4.4. Limitations of the pseudo-random sampling method

The methodology applied in this study tested the underlying assumption that the formation of distinct trace element-to-Ca peaks (Ba/Ca$_{shell}$, Mo/Ca$_{shell}$ and Li/Ca$_{shell}$ peaks) was induced by an enhanced ingestion of trace element-enriched cells of a single or multiple phytoplankton species. Although the pseudo–random sampling method (section 2.5) provides a practical strategy to find potential patterns between a large set of complex phytoplankton time–series and trace element profiles, it also inherits some limitations. (1) The cell concentration data of the various diatom and dinoflagellate species formed the basis of the calculations and were used to quantify the relative abundance of the individual phytoplankton taxa. Accordingly, the method considered the ingestion of phytoplankton cells to be proportional to the number of cells in the water column, without accounting for possible changes in the feeding behavior of the scallops. (2) The simulations considered different time lags between 0 and 50 days by sequentially testing short time windows (3 and 5-day intervals). This technique narrows the maximum time lag difference that two species can hypothetically encounter to a few days, i.e., the duration between the appearance of phytoplankton cells in the water column and the uptake of a particular trace element into the shell between two species can differ only by 3 or 5 days. Consequently, a scenario in which a bloom of one species takes 8 days to be recorded in the shell whereas a bloom of another species needs 20 days, was not encompassed by the simulations. (3) The underlying pathway for the uptake of trace elements is assumed to be similar between the studied years, discarding possible inter–annual differences. In addition, the amount of trace elements at the level of a single phytoplankton cell and/or filtration behavior of the bivalves are likely affected by environmental variables (e.g., currents, salinity, temperature, nutrient availability and dissolved trace element concentration in the surrounding water), which was not considered in the simulations and have to be addressed separately in the future. (4) The temporal resolution of the phytoplankton concentration data differed from that of the trace element profiles and among years, adding challenges to detect and interpret potential patterns between the time-series. The limitations clearly demonstrate the necessity of an ecological interpretation of the obtained results. Despite these constraints, the statistical approach used herein provided the chance to analyze a complex coastal ecosystem and allowed to derive potential relationships between environment and shell chemistry.

5. Summary and conclusions

Based on the results obtained in this study, trace element peaks (Ba/Ca$_{shell}$, Mo/Ca$_{shell}$ and Li/Ca$_{shell}$) in shells of *P. maximus* most likely have a dietary origin that can be related to the activity of individual phytoplankton taxa in the water column. Herein, pseudo-random simulations allowed to decipher this linkage considering various time lags between phytoplankton events and the timing of enhanced trace element incorporation into the shell. The results demonstrated that phytoplankton time-series agreed best to the trace element profiles when a time lag of 8 to 12 days was considered. In other words, the peaks of Ba/Ca$_{shell}$, Mo/

Ca$_{shell}$ and Li/Ca$_{shell}$ show a high degree of similarity to the phytoplankton data when lagged by that time interval. However, potential explanations for the origin of the trace element maxima vary considerably between the different elements. Ba/Ca$_{shell}$ peaks are likely linked to the blooms of ingestible diatoms, dinoflagellates and flagellate. Especially the diatom species *Thalassionema nitzschioides* provided a striking similarity in the timing and magnitude of blooms and the subsequent formation of Ba/Ca$_{shell}$ peaks after 10 days, in all three years. In addition, the simulations indicated that Ba/Ca$_{shell}$ profiles likely have a plurispecific origin, i.e., various phytoplankton taxa enriched in Ba contributed to the measured Ba/Ca$_{shell}$ profiles. However, it remains to be clarified to what extent different taxa control the formation of Ba/Ca$_{shell}$ peaks, which could be tested in subsequent tank experiments by sequentially feeding bivalves with different phytoplankton species and analyzing their geochemical response in the shell carbonate. Measured Mo/Ca$_{shell}$ peaks were shown to be potentially related to the formation of preceding dinoflagellate blooms. In particular, the dinoflagellate species *Gymnodinium* spp. agreed well to the observed Mo/Ca$_{shell}$ profiles when considering the smaller cell size fraction and a small temporal offset. It is hypothesized that the enzyme activity of nitrate reductase, used for nitrate assimilation, triggered the formation of Mo/Ca$_{shell}$ peaks which is shown to be high in *Gymnodinium* spp. cells. In addition to this hypothesis, the results also support the assumption that Mo/Ca$_{shell}$ peaks could be linked to the timing of diatom aggregate formation. Thus, further tank experiments can validate the pathway of Mo from the environment into the shell calcite by, e.g., setting up rolling tanks to simulate aggregate forming and expose the shells to those aggregates, as well as species-specific feeding experiments using *Gymnodinium* spp. cells. In contrast to Ba/Ca$_{shell}$ and Mo/Ca$_{shell}$, the simulations could not establish a clear pattern between phytoplankton and Li/Ca$_{shell}$ peaks. Instead, the data favor two possible scenarios that could describe the formation of Li/Ca$_{shell}$ peaks. On the one hand, the mass occurrence of diatoms, i.e., large bloom of *Chaetoceros* spp., could have favored the accumulation of Li in the shell after a short time lag. On the other hand, a potential link to the formation of harmful diatom blooms could be deduced. As demonstrated, blooms of the diatom *Pseudo-nitzschia* match the timing of Li/Ca$_{shell}$ maxima when a short time lag is implemented in the model. Since not all *Pseudo-nitzschia* blooms could be associated with a Li/Ca$_{shell}$ peak, it is proposed that the synthesis of the neurotoxin domoic acid is linked to stressful conditions in the ambient water such as nutrient limitation and/or high grazing activity of zooplankton. This toxin sequesters Li which is then ingested by scallop and potentially accounts for the enrichment of Li in the shell. Shells from additional years with transient Li/Ca$_{shell}$ peaks are required to confirm either of these hypotheses as a large Li/Ca$_{shell}$ maximum was only measured in one of the three studied years. If the demonstrated assumptions can be further developed and verified, Ba/Ca$_{shell}$, Mo/Ca$_{shell}$ and Li/Ca$_{shell}$ profiles will establish powerful proxies to reconstruct past phytoplankton dynamics that prevailed in the water column. Ba/Ca$_{shell}$ peaks could then be utilized as plurispecific indicators for the timing and magnitude of phytoplankton species enriched in Ba. Mo/Ca$_{shell}$ profiles will establish a powerful tool to assess dynamics of specific dinoflagellate species growing on nitrates or the timing of diatom aggregate formation. Finally, the Li/Ca$_{shell}$ peaks can reveal information about large diatom blooms or the timing and frequency of toxic diatom blooms as well as periods of enhanced zooplankton activity in the water column.

CRediT authorship contribution statement

Lukas Fröhlich: Conceptualization, Formal analysis, Investigation, Methodology, Visualization, Writing – original draft, Writing – review & editing. **Valentin Siebert:** Investigation, Formal analysis, Writing – review & editing. **Qian Huang:** Conceptualization, Methodology, Formal analysis, Supervision, Writing – review & editing. **Julien Thébault:** Project administration, Investigation, Resources, Validation, Supervision, Writing – review & editing. **Klaus Peter Jochum:**

Resources, Validation, Writing – review & editing. **Bernd R. Schöne:** Resources, Conceptualization, Formal analysis, Funding acquisition, Supervision, Validation, Writing – original draft, Writing – review & editing.

Declaration of Competing Interest

The authors declare that they have no known competing financial interests or personal relationships that could have appeared to influence the work reported in this paper.

Data availability

Data will be made available on request.

Appendix A. Supplementary data

Supplementary data to this article can be found online at https://doi.org/10.1016/j.ecolind.2022.109121.

References

Alldredge, A.L., Gotschalk, C.C., 1989. Direct observations of the mass flocculation of diatom blooms: characteristics, settling velocities and formation of diatom aggregates. Deep Sea Res. Part A Oceanogr. Res. Pap. 36, 159–171. https://doi.org/10.1016/0198-0149(89)90131-3.

Barats, A., Amouroux, D., Chauvaud, L., Pécheyran, C., Lorrain, A., Thébault, J., Church, T.M., Donard, O.F.X., 2009. High frequency Barium profiles in shells of the Great Scallop *Pecten maximus*: A methodical long-term and multi-site survey in Western Europe. Biogeosciences 6, 157–170. https://doi.org/10.5194/bg-6-157-2009.

Barats, A., Amouroux, D., Pécheyran, C., Chauvaud, L., Thébault, J., Donard, X.O.F., 2010. Spring molybdenum enrichment in scallop shells: A potential tracer of diatom productivity in temperate coastal environments (Brittany, NW France). Biogeosciences 7, 233–245. https://doi.org/10.5194/bg-7-233-2010.

Barats, A., Pécheyran, C., Amouroux, D., Dubascoux, S., Chauvaud, L., Donard, O.F.X., 2007. Matrix-matched quantitative analysis of trace-elements in calcium carbonate shells by laser-ablation ICP-MS: Application to the determination of daily scale profiles in scallop shell (*Pecten maximus*). Anal. Bioanal. Chem. 387, 1131–1140. https://doi.org/10.1007/s00216-006-0954-8.

Barbier, E.B., Hacker, S.D., Kennedy, C., Koch, E.W., Stier, A.C., Silliman, B.R., 2011. The value of estuarine and coastal ecosystem services. Ecol. Monogr. 81, 169–193. https://doi.org/10.1890/10-1510.1.

Bates, S.S., Bird, C.J., de Freitas, A.S.W., Foxall, R., Gilgan, M., Hanic, L.A., Johnson, G. R., McCulloch, A.W., Odense, P., Pocklington, R., Quilliam, M.A., Sim, P.G., Smith, J. C., Subba Rao, D.V., Todd, E.C.D., Walter, J.A., Wright, J.L.C., 1989. Pennate diatom *Nitzschia pungens* as the primary source of domoic acid, a toxin in shellfish from eastern Prince Edward Island, Canada. Can. J. Fish. Aquat. Sci. 46, 1203–1215. https://doi.org/10.1139/f89-156.

Bates, S.S., Hubbard, K.A., Lundholm, N., Montresor, M., Leaw, C.P., 2018. *Pseudo-nitzschia, Nitzschia*, and domoic acid: New research since 2011. Harmful Algae 79, 3–43. https://doi.org/10.1016/j.hal.2018.06.001.

Beman, J.M., Arrigo, K.R., Matson, P.A., 2005. Agricultural runoff fuels large phytoplankton blooms in vulnerable areas of the ocean. Nature 434, 211–214. https://doi.org/10.1038/nature03370.

Beninger, P.G., Decottignies, P., Rincé, Y., 2004. Localization of qualitative particle selection sites in the heterorhabdic filibranch *Pecten maximus* (Bivalvia: Pectinidae). Mar. Ecol. Prog. Ser. 275, 163–173. https://doi.org/10.3354/meps275163.

Bienfang, P.K., 1981. Sinking rates of heterogeneous, temperate phytoplankton populations. J. Plankton Res. 3, 235–253. https://doi.org/10.1093/plankt/3.2.235.

Bienfang, P.K., Harrison, P.J., Quarmby, L.M., 1982. Sinking rate response to depletion of nitrate, phosphate and silicate in four marine diatoms. Mar. Biol. 67, 295–302. https://doi.org/10.1007/BF00397670.

Bishop, J.K.B., 1988. The barite-opal-organic carbon association in oceanic particulate matter. Nature 332, 341–343. https://doi.org/10.1038/332341a0.

Cardinale, B.J., Srivastava, D.S., Duffy, J.E., Wright, J.P., Downing, A.L., Sankaran, M., Jouseau, C., 2006. Effects of biodiversity on the functioning of trophic groups and ecosystems. Nature 443, 989–992. https://doi.org/10.1038/nature05202.

Chauvaud, L., Donval, A., Paulet, Y., 2001. Variations in food intake of *Pecten maximus* (L.) from the Bay of Brest (France): Influence of environmental factors and phytoplankton species composition. C.R. Acad. Sci. 324, 1–13. https://doi.org/10.1016/S0764-4469(01)01349-X.

Chauvaud, L., Jean, F., Ragueneau, O., Thouzeau, G., 2000. Long-term variation of the Bay of Brest ecosystem: Benthic-pelagic coupling revisited. Mar. Ecol. Prog. Ser. 200, 35–48. https://doi.org/10.3354/meps200035.

Chauvaud, L., Lorrain, A., Dunbar, R.B., Paulet, Y.M., Thouzeau, G., Jean, F., Guarini, J. M., Mucciarone, D., 2005. Shell of the Great Scallop *Pecten maximus* as a high-frequency archive of paleoenvironmental changes. Geochem. Geophys. Geosyst. 6, 1–15. https://doi.org/10.1029/2004GC000890.

Chauvaud, L., Thébault, J., Clavier, J., Lorrain, A., Strand, Ø., 2011. What's hiding behind ontogenetic δ13C variations in mollusk shells? New insights from the Great Scallop (*Pecten maximus*). Estuaries Coasts 34, 211–220. https://doi.org/10.1007/s12237-010-9267-4.

Chauvaud, L., Thouzeau, G., Paulet, Y.M., 1998. Effects of environmental factors on the daily growth rate of *Pecten maximus* juveniles in the Bay of Brest (France). J. Exp. Mar. Bio. Ecol. 227, 83–111. https://doi.org/10.1016/S0022-0981(97)00263-3.

Cloern, J.E., 2001. Our evolving conceptual model of the coastal eutrophication problem. Mar. Ecol. Prog. Ser. 210, 223–253. https://doi.org/10.3354/MEPS210223.

Collier, R.W., 1985. Molybdenum in the Northeast Pacific Ocean. Limnol. Oceanogr. 30, 1351–1354. https://doi.org/10.4319/LO.1985.30.6.1351.

Corzo, A., Morillo, J.A., Rodríguez, S., 2000. Production of transparent exopolymer particles (TEP) in cultures of *Chaetoceros calcitrans* under nitrogen limitation. Aquat. Microb. Ecol. 23, 63–72. https://doi.org/10.3354/AME023063.

Dehairs, F., Chesselet, R., Jedwab, J., 1980. Discrete suspended particles of barite and the barium cycle in the open ocean. Earth Planet. Sci. Lett. 49, 528–550. https://doi.org/10.1016/0012-821X(80)90094-1.

Del Amo, Y., Quéguiner, B., Tréguer, P., Breton, H., Lampert, L., 1997. Impacts of high-nitrate freshwater inputs on macrotidal ecosystems. II. Specific role of the silicic acid pump in the year-round dominance of diatoms in the Bay of Brest (France). Mar. Ecol. Prog. Ser. 161, 225–237. https://doi.org/10.3354/meps161225.

Desortová, B., 1981. Relationship between chlorophyll-a concentration and phytoplankton biomass in several reservoirs in Czechoslovakia. Int. Revue ges. Hydrobiol. Hydrogr. 66, 153–169. https://doi.org/10.1002/iroh.19810660202.

Doré, J., Chaillou, G., Poitevin, P., Lazure, P., Poirier, A., Chauvaud, L., Archambault, P., Thébault, J., 2020. Assessment of Ba/Ca in *Arctica islandica* shells as a proxy for phytoplankton dynamics in the Northwestern Atlantic Ocean. Estuar. Coast. Shelf Sci. 237, 106628 https://doi.org/10.1016/j.ecss.2020.106628.

Dymond, J., Collier, R., McManus, J., Honjo, S., Manganini, S., 1997. Can the aluminum and titanium contents of ocean sediments be used to determine the paleoproductivity of the oceans? Paleoceanography 12, 586–593. https://doi.org/10.1029/97PA01135.

Eppley, R.W., Coatsworth, J.L., 1968. Uptake of nitrate and nitrite by *Ditylum brightwellii*-kinetics and mechanisms. J. Phycol. 4, 151–156. https://doi.org/10.1111/j.1529-8817.1968.tb04689.x.

Eppley, R.W., Coatsworth, J.L., Solórzano, L., 1969. Studies of Nitrate Reductase in Marine Phytoplankton. Limnol. Oceanogr. 14, 194–205. https://doi.org/10.4319/lo.1969.14.2.0194.

Field, C.B., Behrenfeld, M.J., Randerson, J.T., Falkowski, P., 1998. Primary production of the biosphere: Integrating terrestrial and oceanic components. Science 281, 237–240. https://doi.org/10.1126/science.281.5374.237.

Fisher, N.S., Guillard, R.R.L., Bankston, D.C., 1991. The accumulation of barium by marine phytoplankton grown in culture. J. Mar. Res. 49, 339–354. https://doi.org/10.1357/002224091784995882.

Fröhlich, L., Siebert, V., Walliser, E.O., Thébault, J., Jochum, K.P., Chauvaud, L., Schöne, B.R., 2022. Ba/Ca profiles in shells of *Pecten maximus* – A proxy for specific primary producers rather than bulk phytoplankton. Chem. Geol. 593, 120743 https://doi.org/10.1016/J.CHEMGEO.2022.120743.

Gillikin, D.P., Dehairs, F., Lorrain, A., Steenmans, D., Baeyens, W., André, L., 2006. Barium uptake into the shells of the common mussel (*Mytilus edulis*) and the potential for estuarine paleo-chemistry reconstruction. Geochim. Cosmochim. Acta 70, 395–407. https://doi.org/10.1016/j.gca.2005.09.015.

Gillikin, D.P., Lorrain, A., Paulet, Y.M., André, L., Dehairs, F., 2008. Synchronous barium peaks in high-resolution profiles of calcite and aragonite marine bivalve shells. Geo-Marine Lett. 28, 351–358. https://doi.org/10.1007/s00367-008-0111-9.

Gordon, H.R., Clark, D.K., Mueller, J.L., Hovis, W.A., 1980. Phytoplankton pigments from the nimbus-7 coastal zone color scanner: Comparisons with surface measurements. Science 210, 63–66. https://doi.org/10.1126/science.210.4465.63.

Hallmann, N., Schöne, B.R., Strom, A., Fiebig, J., 2008. An intractable climate archive – Sclerochronological and shell oxygen isotope analyses of the Pacific geoduck, *Panopea abrupta* (bivalve mollusk) from Protection Island (Washington State, USA).

Palaeogeogr. Palaeoclimatol. Palaeoecol. 269, 115–126. https://doi.org/10.1016/j.palaeo.2008.08.010.

Hare, C.E., Leblanc, K., DiTullio, G.R., Kudela, R.M., Zhang, Y., Lee, P.A., Riseman, S., Hutchins, D.A., 2007. Consequences of increased temperature and CO2 for phytoplankton community structure in the Bering Sea. Mar. Ecol. Prog. Ser. 352, 9–16. https://doi.org/10.3354/MEPS07182.

Harrison, W.G., 1973. Nitrate Reductase Activity During a Dinoflagellate Bloom. Limnol. Oceanogr. 18, 457–465. https://doi.org/10.4319/lo.1973.18.3.0457.

Hatch, M.B.A., Schellenberg, S.A., Carter, M.L., 2013. Ba/Ca variations in the modern intertidal bean clam *Donax gouldii*: An upwelling proxy? Palaeogeogr. Palaeoclimatol. Palaeoecol. 373, 98–107. https://doi.org/10.1016/j.palaeo.2012.03.006.

Ho, T.Y., Quigg, A., Finkel, Z.V., Milligan, A.J., Wyman, K., Falkowski, P.G., Morel, F.M. M., 2003. The elemental composition of some marine phytoplankton. J. Phycol. 39, 1145–1159. https://doi.org/10.1111/j.0022-3646.2003.03-090.x.

Hovis, W.A., Clark, D.K., Anderson, F., Austin, R.W., Wilson, W.H., Baker, E.T., Ball, D., Gordon, H.R., Mueller, J.L., El-Sayed, S.Z., Sturm, B., Wrigley, R.C., Yentsch, C.S., 1980. Nimbus-7 coastal zone color scanner: System description and initial imagery. Science 210, 60–63. https://doi.org/10.1126/science.210.4465.60.

Iglesias-Rodriguez, M.D., Halloran, P.R., Rickaby, R.E.M., Hall, I.R., Colmenero-Hidalgo, E., Gittins, J.R., Green, D.R.H., Tyrrell, T., Gibbs, S.J., Von Dassow, P., Rehm, E., Armbrust, E.V., Boessenkool, K.P., 2008. Phytoplankton calcification in a high-CO₂ world. Science 320, 336–340. https://doi.org/10.1126/science.1154122.

Jochum, K.P., Garbe-Schönberg, D., Veter, M., Stoll, B., Weis, U., Weber, M., Lugli, F., Jentzen, A., Schiebel, R., Wassenburg, J.A., Jacob, D.E., Haug, G.H., 2019. Nano-Powdered Calcium Carbonate Reference Materials: Significant Progress for Microanalysis? Geostand. Geoanalytical Res. 43, 595–609. https://doi.org/10.1111/ggr.12292.

Jochum, K.P., Stoll, B., Herwig, K., Willbold, M., 2007. Validation of LA-ICP-MS trace element analysis of geological glasses using a new solid-state 193 nm Nd:YAG laser and matrix-matched calibration. J. Anal. At. Spectrom. 22, 112–121. https://doi.org/10.1039/b609547j.

Jochum, K.P., Weis, U., Stoll, B., Kuzmin, D., Yang, Q., Raczek, I., Jacob, D.E., Stracke, A., Birbaum, K., Frick, D.A., Günther, D., Enzweiler, J., 2011. Determination of reference values for NIST SRM 610–617 glasses following ISO guidelines. Geostand. Geoanalytical Res. 35, 397–429. https://doi.org/10.1111/j.1751-908X.2011.00120.x.

Kruskopf, M., Flynn, K.J., 2006. Chlorophyll content and fluorescence responses cannot be used to gauge reliably phytoplankton biomass, nutrient status or growth rate. New Phytol. 169, 525–536. https://doi.org/10.1111/j.1469-8137.2005.01601.x.

Lionard, M., Muylaert, K., Tackx, M., Vyverman, W., 2008. Evaluation of the performance of HPLC-CHEMTAX analysis for determining phytoplankton biomass and composition in a turbid estuary (Schelde, Belgium). Estuar. Coast. Shelf Sci. 76, 809–817. https://doi.org/10.1016/J.ECSS.2007.08.003.

Longerich, H.P., Jackson, S.E., Günther, D., 1996. Laser ablation inductively coupled plasma mass spectrometric transient signal data acquisition and analyte concentration calculation. J. Anal. At. Spectrom. 11, 899–904. https://doi.org/10.1039/JA9961100899.

Lorenzen, C.J., 1967. Vertical distribution of chlorophyll and phaeo-pigments: Baja California. Deep. Res. Oceanogr. Abstr. 14, 735–745. https://doi.org/10.1016/S0011-7471(67)80010-X.

Lorenzen, C.J., 1966. A method for the continuous measurement of *in vivo* chlorophyll concentration. Deep. Res. Oceanogr. Abstr. 13, 223–227. https://doi.org/10.1016/0011-7471(66)91102-8.

Lorrain, A., Paulet, Y.M., Chauvaud, L., Savoye, N., Nézan, E., Guérin, L., 2000. Growth anomalies in *Pecten maximus* from coastal waters (Bay of Brest, France): Relationship with diatom blooms. J. Mar. Biol. Assoc. United Kingdom 80, 667–673. https://doi.org/10.1017/S0025315400002496.

Marali, S., Schöne, B.R., Mertz-Kraus, R., Griffin, S.M., Wanamaker, A.D., Matras, U., Butler, P.G., 2017. Ba/Ca ratios in shells of *Arctica islandica*—Potential environmental proxy and crossdating tool. Palaeogeogr. Palaeoclimatol. Palaeoecol. 465, 347–361. https://doi.org/10.1016/j.palaeo.2015.12.018.

Marino, R., Howarth, R.W., Chan, F., Cole, J.J., Likens, G.E., 2003. Sulfate inhibition of molybdenum-dependent nitrogen fixation by planktonic cyanobacteria under seawater conditions: A non-reversible effect. Hydrobiologia 500, 277–293. https://doi.org/10.1023/A:1024641904568.

Marinov, I., Doney, S.C., Lima, I.D., 2010. Response of ocean phytoplankton community structure to climate change over the 21st century: Partitioning the effects of nutrients, temperature and light. Biogeosciences 7, 3941–3959. https://doi.org/10.5194/BG-7-3941-2010.

Martin, J.H., Knauer, G.A., 1973. The elemental composition of plankton. Geochim. Cosmochim. Acta 37, 1639–1653. https://doi.org/10.1016/0016-7037(73)90154-3.

Morris, I., Syrett, P.J., 1963. The development of nitrate reductase in *Chlorella* and its repression by ammonium. Arch. Mikrobiol. 47, 32–41. https://doi.org/10.1007/BF00408287.

Nashad, M., Nandini Menon, N., Ajith Joseph, C., Pettersson, L.H., Menon, N.R., 2017. First report of *Leptocylindrus* sp. bloom in the coastal waters of Kerala, southeast Arabian Sea. J. Mar. Biol. Assoc. India 59, 87–92. https://doi.org/10.6024/jmbai.2017.59.1.1937-13.

Nixon, S.W., 1995. Coastal marine eutrophication: A definition, social causes, and future concerns. Ophelia 41, 199–219. https://doi.org/10.1080/00785236.1995.10422044.

Pan, Y., Subba Rao, D.V., Mann, K.H., Li, W.K.W., Harrison, W.G., 1996. Effects of silicate limitation on production of domoic acid, a neurotoxin, by the diatom *Pseudo-nitzschia multiseries*. II. Continuous culture studies. Mar. Ecol. Prog. Ser. 131, 235–243. https://doi.org/10.3354/MEPS131235.

Peperzak, L., Colijn, F., Koeman, R., Gieskes, W.W.C., Joordens, J.C.A., 2003. Phytoplankton sinking rates in the rhine region of freshwater influence. J. Plankton Res. 25, 365–383. https://doi.org/10.1093/plankt/25.4.365.

Radach, G., Berg, J., Hagmeier, E., 1990. Long-term changes of the annual cycles of meteorological, hydrographic, nutrient and phytoplankton time series at Helgoland and at LV ELBE 1 in the German Bight. Cont. Shelf Res. 10, 305–328. https://doi.org/10.1016/0278-4343(90)90054-P.

Ragueneau, O., Varela, E.D., Treguer, P., Queguiner, B., Delamo, Y., 1994. Phytoplankton dynamics in relation to the biogeochemical cycle of silicon in a coastal ecosystem of Western Europe. Mar. Ecol. Prog. Ser. 106, 157–172. https://doi.org/10.3354/meps106157.

Richardson, C.A., Crisp, D.J., Runham, N.W., 1980. An endogenous rhythm in shell deposition in *Cerastoderma edule*. J. Mar. Biol. Assoc. United Kingdom 60, 991–1004. https://doi.org/10.1017/S0025315400042041.

Richardson, K., Heilmann, J., 1995. Primary production in the Kattegat: Past and present. Ophelia 41, 317–328. https://doi.org/10.1080/00785236.1995.10422050.

Roth, I., Riley, J.P., 1971. The distribution of trace elements in some species of phytoplankton grown in culture. J. Mar. Biol. Assoc. United Kingdom 51, 63–72. https://doi.org/10.1017/S0025315400006457.

Schöne, B.R., 2008. The curse of physiology – Challenges and opportunities in the interpretation of geochemical data from mollusk shells. Geo-Marine Lett. 28, 269–285. https://doi.org/10.1007/s00367-008-0114-6.

Shumway, S.E., Cucci, T.L., Lesser, M.P., Bourne, N., Bunting, B., 1997. Particle clearance and selection in three species of juvenile scallops. Aquac. Int. 5, 89–99. https://doi.org/10.1007/BF02764790.

Shuter, B., 1979. A model of physiological adaptation in unicellular algae. J. Theor. Biol. 78, 519–552. https://doi.org/10.1016/0022-5193(79)90189-9.

Sigman, D.M., Boyle, E.A., 2000. Glacial/interglacial variations in atmospheric carbon dioxide. Nature 407, 859–869. https://doi.org/10.2143/TVG.60.19.1001996.

Smith, V.H., 2003. Eutrophication of freshwater and coastal marine ecosystems: A global problem. Environ. Sci. Pollut. Res. 10, 126–139. https://doi.org/10.1065/espr2002.12.142.

Stecher, H.A., Krantz, D.E., Lord, C.J., Luther, G.W., Bock, K.W., 1996. Profiles of strontium and barium in *Mercenaria mercenaria* and *Spisula solidissima* shells. Geochim. Cosmochim. Acta 60, 3445–3456. https://doi.org/10.1016/0016-7037(96)00179-2.

Sternberg, E., Tang, D., Ho, T.Y., Jeandel, C., Morel, F.M.M., 2005. Barium uptake and adsorption in diatoms. Geochim. Cosmochim. Acta 69, 2745–2752. https://doi.org/10.1016/j.gca.2004.11.026.

Strom, S.L., 1993. Production of pheopigments by marine protozoa: results of laboratory experiments analysed by HPLC. Deep. Res. Part I 40, 57–80. https://doi.org/10.1016/0967-0637(93)90053-6.

Subba Rao, D.V., Pan, Y., Mukhida, K., 1998. Production of domoic acid by *Pseudo-nitzschia multiseries* Hasle, affected by lithium. Mar. Ecol. 19, 31–36. https://doi.org/10.1111/j.1439-0485.1998.tb00451.x.

Tabouret, H., Pomerleau, S., Jolivet, A., Pécheyran, C., Riso, R., Thébault, J., Chauvaud, L., Amouroux, D., 2012. Specific pathways for the incorporation of dissolved barium and molybdenum into the bivalve shell: An isotopic tracer approach in the juvenile Great Scallop (*Pecten maximus*). Mar. Environ. Res. 78, 15–25. https://doi.org/10.1016/j.marenvres.2012.03.006.

Thébault, J., Chauvaud, L., 2013. Li/Ca enrichments in great scallop shells (*Pecten maximus*) and their relationship with phytoplankton blooms. Palaeogeogr. Palaeoclimatol. Palaeoecol. 373, 108–122. https://doi.org/10.1016/j.palaeo.2011.12.014.

Thébault, J., Chauvaud, L., Clavier, J., Fichez, R., Morize, E., 2006. Evidence of a 2-day periodicity of striae formation in the tropical scallop *Comptopallium radula* using calcein marking. Mar. Biol. 149, 257–267. https://doi.org/10.1007/s00227-005-0198-8.

Thébault, J., Chauvaud, L., L'Helguen, S., Clavier, J., Barats, A., Jacquet, S., Pécheyran, C., Amouroux, D., 2009. Barium and molybdenum records in bivalve shells: Geochemical proxies for phytoplankton dynamics in coastal environments? Limnol. Oceanogr. 54, 1002–1014. https://doi.org/10.4319/lo.2009.54.3.1002.

Thébault, J., Jolivet, A., Waeles, M., Tabouret, H., Sabarot, S., Pécheyran, C., Leynaert, A., Jochum, K.P., Schöne, B.R., Fröhlich, L., Siebert, V., Amice, E., Chauvaud, L., 2022. Scallop shells as geochemical archives of phytoplankton-related ecological processes in a temperate coastal ecosystem. Limnol. Oceanogr. 67, 187–202. https://doi.org/10.1002/lno.11985.

Thornton, D.C.O., 2002. Diatom aggregation in the sea: mechanisms and ecological implications. Eur. J. Phycol. 37, 149–161. https://doi.org/10.1017/S0967026202003657.

Vander Putten, E., Dehairs, F., Keppens, E., Baeyens, W., 2000. High resolution distribution of trace elements in the calcite shell layer of modern *Mytilus edulis*: Environmental and biological controls. Geochim. Cosmochim. Acta 64, 997–1011. https://doi.org/10.1016/S0016-7037(99)00380-4.

Wang, J.X., Kong, F.Z., Geng, H.X., Zhang, Q.C., Yuan, Y.Q., Yu, R.C., 2021. CHEMTAX analysis of phytoplankton assemblages revealed potential indicators for blooms of haptophyte Phaeocystis globosa. Ecol. Ind. 131, 108177 https://doi.org/10.1016/J.ECOLIND.2021.108177.

Warner, A.J., Hays, G.C., 1994. Sampling by the continuous plankton recorder survey. Prog. Oceanogr. 34, 237–256. https://doi.org/10.1016/0079-6611(94)90011-6.

Westberry, T., Behrenfeld, M.J., Siegel, D.A., Boss, E., 2008. Carbon-based primary productivity modeling with vertically resolved photoacclimation. Global Biogeochem. Cycles 22, 1–18. https://doi.org/10.1029/2007GB003078.

Widdows, J., Moore, M.N., Lowe, D.M., Salkeld, P.N., 1979. Some effects of a dinoflagellate bloom (*Gyrodinium aureolum*) on the mussel, *Mytilus edulis*. J. Mar.

Biol. Assoc. United Kingdom 59, 522–524. https://doi.org/10.1017/S0025315400042843.

Wiltshire, K.H., Manly, B.F.J., 2004. The warming trend at Helgoland Roads, North Sea: Phytoplankton response. Helgol. Mar. Res. 58, 269–273. https://doi.org/10.1007/s10152-004-0196-0.

Winder, M., Sommer, U., 2012. Phytoplankton response to a changing climate. Hydrobiologia 698, 5–16. https://doi.org/10.1007/s10750-012-1149-2.

Worm, B., Barbier, E.B., Beaumont, N., Duffy, J.E., Folke, C., Halpern, B.S., Jackson, J.B. C., Lotze, H.K., Micheli, F., Palumbi, S.R., Sala, E., Selkoe, K.A., Stachowicz, J.J., Watson, R., 2006. Impacts of biodiversity loss on ocean ecosystem services. Science 314, 787–790. https://doi.org/10.1126/science.1132294.

Wright, S.W., van den Enden, R.L., Pearce, I., Davidson, A.T., Scott, F.J., Westwood, K.J., 2010. Phytoplankton community structure and stocks in the Southern Ocean (30–80°E) determined by CHEMTAX analysis of HPLC pigment signatures. Deep Sea Res. Part II Top. Stud. Oceanogr. 57, 758–778. https://doi.org/10.1016/J.DSR2.2009.06.015.

Yamamoto, T., Oh, S.J., Kataoka, Y., 2004. Growth and uptake kinetics for nitrate, ammonium and phosphate by the toxic dinoflagellate *Gymnodinium catenatum* isolated from Hiroshima Bay, Japan. Fish. Sci. 70, 108–115. https://doi.org/10.1111/j.1444-2906.2003.00778.x.